

Repulsive particle interactions enable selective information processing at cellular interfaces

J. Elliott^{1,2}, H. Shah¹, R. Belousov¹, G. Dey¹, and A. Erzberger^{1,2,*}

¹Cell Biology and Biophysics Unit, European Molecular Biology Laboratory, Meyerhofstraße 1, 69117 Heidelberg, Germany

²Department of Physics and Astronomy, Heidelberg University, 69120 Heidelberg, Germany

(Dated: June 18, 2025)

Living systems relay information across membrane interfaces to coordinate compartment functions. We identify a physical mechanism for selective information transmission that arises from the sigmoidal response of surface-bound particle densities to spatial features of adjacent external structures. This mechanism implements a form of spatial thresholding, enabling the binary classification of external cues. Expansion microscopy measurements of nuclear pore complex distributions in *S. arctica* show signatures of such physical thresholding.

Living systems process information to adapt and respond to their environment [1–5]. Theoretical principles underlying biological information processing have been identified in gene regulation [6, 7], biochemical signaling [8–13], and cell-fate patterning [14–21]. Yet beyond molecular circuits, *physical* interactions, mechanical properties, and geometrical relations also impact how living materials process information [22–31]. Physical degrees of freedom influence how cells navigate complex environments [32–36], internalize pathogens [37–39], or coordinate subcellular processes [23, 40, 41]. For example, migrating cells respond to gradients in the elastic properties of structures in their environment (durotaxis [42, 43]), or the density of binding sites for specific adhesion molecules (haptotaxis, [42, 44–46]) using biophysical interactions between adhesion molecules, cell membrane, cytoskeleton, and external binding sites to read out information about external spatial heterogeneities. However, the principles underlying such physically mediated signal processing are not well understood [47, 48]. In particular, how physical interactions shape the encoding and transmission of spatially-resolved mechanical signals is unclear.

In this letter, we focus on physical interactions of surface-embedded particles at the interfaces of biological, membrane-enclosed systems [Fig. 1(a)]. We investigate how the spatial distribution of such particles selectively encodes information stored in the features of surrounding external structures, e.g. the proximity of binding sites, which can subsequently change internal cellular states such as polarity [49]. We identify how nonlinear relations due to particle interactions control the flow of information across the interface, whereby the interface itself functions as an information-processing layer in a hierarchical architecture.

Specifically, we find that particle interactions of the simplest type—short-range repulsion—create sigmoidal mappings between an input potential field and output particle distribution, providing a physical mechanism for *binary thresholding* reminiscent of thresholding filters in

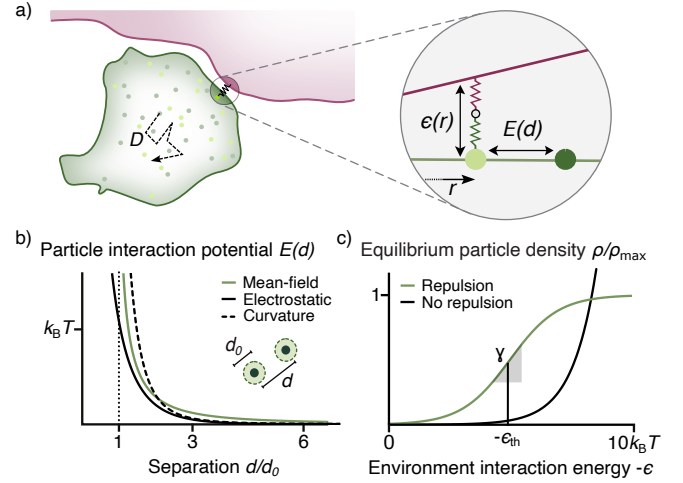


FIG. 1. The density of repulsive particles responds nonlinearly to changes in binding energy. a) Particles on the surface of a membrane-enclosed compartment interact via a potential $E(d)$ that depends on their average separation distance d . Each particle can be either bound (light green circles) to an external structure (purple) or unbound (dark green circles), with binding rates set by a non-uniform interaction energy field ϵ . b) The mean-field potential $E(d)$ captures short-range repulsion due to steric effects between particles of diameter d_0 , similar to curvature-mediated interactions and shielded electrostatic repulsion [50–57, Supplementary Materials Sec. A b]. c) Repulsive particle interactions lead to a sigmoidal equilibrium density profile in response to changes in the particle-environment interaction energy ϵ , approaching the maximum density ρ_{\max} , in contrast to ideal, non-repulsive particles. Vertical line and shaded triangle show the threshold ϵ_{th} and gain γ of the sigmoid.

computer vision [58]. By deriving explicit expressions for the *gain* and *threshold* parameters of the filter, we identify how the system’s physical properties, i.e. the effective size of the surface-embedded particles and their typical concentrations, control the transfer of information. We identify an optimal information-processing regime and find that diverse interface-associated protein complexes and macromolecular structures in cells operate within this regime. In particular, we experimentally mea-

* erzberge@embl.de

sure the predicted sigmoidal distribution of nuclear pore complexes in the envelope of *Sphaeroforma arctica* nuclei [59], which form in response to interactions with the surrounding cytoskeleton [60]. Our results indicate that physical thresholding could facilitate information transmission in the coordination of biological processes across cellular and subcellular interfaces.

Repulsive particle interactions binarize binding energy profiles.—We consider diffusive particles on a membrane, which interact with the environment by attaching to and detaching from adjacent binding sites. The densities of particles ρ_i in the bound ($i = b$) and unbound ($i = u$) states, with state energies ϵ_i , evolve according to mass-conserving reaction-diffusion equations [61–63]

$$\partial_t \rho_i = \nabla \cdot [D_i \nabla \rho_i + \beta D_i \rho_i \nabla (E + \epsilon_i)] + \mathcal{R}_i \quad (1)$$

driven by a mean-field interaction potential $E(\rho)$, which depends on the total density $\rho = \rho_b + \rho_u$, with the inverse thermal energy scale $\beta = (k_B T)^{-1}$ and, in general, density-dependent diffusion coefficients D_i [64]. The reaction terms describe transitions between the two states according to $\mathcal{R}_u = -\mathcal{R}_b = k_{\text{off}} \rho_b - k_{\text{on}} \rho_u$. To investigate how spatial heterogeneities in the environment influence the particle distribution, we consider nonuniform attachment rates $k_{\text{on}} = k_{\text{off}} e^{-\beta \epsilon}$, in which $\epsilon(\mathbf{r}) = \epsilon_b - \epsilon_u$ is a particle-environment binding energy field.

From Eq. (1) and assuming no-flux boundary conditions, we obtain the *equilibrium* total density [65, Supplementary Materials Sec. A]

$$\rho = \frac{1}{l^2} e^{-\beta E(\rho)} \left(1 + e^{-\beta \epsilon(\mathbf{r})} \right), \quad (2)$$

where the integration constant l is a length-scale set by the conservation of the total particle number N over the whole membrane area A according to

$$N = \int_A dA \rho. \quad (3)$$

Equation (2) describes how the distribution of particles on the membrane surface responds to heterogeneities in mechanical and/or chemical properties of external structures, which give rise to a non-uniform $\epsilon(\mathbf{r})$. An effective Hookean interaction energy can, for example, characterize the interactions of membrane-associated particles with external structures at a variable separation distance $h(\mathbf{r})$

$$\epsilon(\mathbf{r}) = \frac{\lambda}{2} h(\mathbf{r})^2 + \epsilon_c, \quad (4)$$

such that the non-uniform interaction energy captures spatial variations in binding site proximity. Heterogeneities in the chemical or elastic properties of the environment might furthermore introduce a non-uniform ϵ_c and/or effective spring constant λ .

Interparticle interactions influence how the density (2) responds to such external heterogeneities. Focusing on

steric interactions [Supplementary Materials Sec. B b], we impose that each particle occupies an area d_0^2 , and obtain the mean-field potential [Supplementary Materials Eq. (S28)]

$$E(\rho) = -k_B T \ln(1 - d_0^2 \rho) \quad (5)$$

which corresponds to the chemical potential difference between a volume-excluding lattice gas and the ideal gas [66, 67]. Equation (5) approximates well short-range potentials e.g. from curvature-mediated or shielded electrostatic interactions (Fig. 1(b)).

The equilibrium particle distribution resulting from Eqs. (2) and (5)

$$\rho(\mathbf{r}) = \frac{1 + e^{-\beta \epsilon(\mathbf{r})}}{l^2 + d_0^2 (1 + e^{-\beta \epsilon(\mathbf{r})})}, \quad (6)$$

corresponds to a sigmoidal mapping between the binding energy field $\epsilon(\mathbf{r})$ and the density $\rho(\mathbf{r})$ [Fig. 1(c)]. In fact, we recover a Fermi-Dirac-like distribution, where the particle density at different positions is akin to the occupation number of energy levels, which are resolved along the surface according to $\epsilon(\mathbf{r})$: particles occupy the most energetically favorable spatial positions, given steric interactions and subject to mass-conservation, leading to regions of high and low density. Therefore, the resulting particle distribution sigmoidally *filters* external heterogeneities, providing a physical mechanism for binarizing the binding-energy field. A cellular or subcellular interface could thereby read out spatial variations in, for example, the proximity of nearby structures.

The sigmoidal relation Eq. (6) is characterized by the gain γ and the threshold ϵ_{th} [Fig. 1(c)], given by

$$\gamma := \max \left(\left\| \frac{\partial \rho}{\partial \epsilon} \right\| \right) = \frac{\beta l^2}{4 d_0^2 (d_0^2 + l^2)}, \quad (7)$$

and

$$\epsilon_{\text{th}} := \text{argmax} \left(\left\| \frac{\partial \rho}{\partial \epsilon} \right\| \right) = k_B T \ln \left(\frac{d_0^2}{d_0^2 + l^2} \right), \quad (8)$$

which depend on two length scales: the effective particle size d_0 , and the average particle separation across the whole surface $\bar{d} = \sqrt{A/N}$. The former determines the maximum possible density of the particles $\rho_{\text{max}} = 1/d_0^2$, whereas the latter is set by the area of the membrane, and the total number of embedded particles, via the constraint Eq. (3). Through the integral over the entire membrane surface, this constraint incorporates a global dependence of the particle distribution on the interaction energy field into the normalization constant l , whose explicit expression follows $l \propto \sqrt{\bar{d}^2 - d_0^2}$ for uniform ϵ .

Particle size and total number tune information transmission.—Could cells use Eq. (6) to sense the proximity of nearby structures? To investigate how the distance between a membrane patch and an adjacent set of binding

sites can be conveyed by the particle density, we analyze the transmission of information in the presence of fluctuations.

In general, a noisy sigmoidal response can amplify an input signal close to the threshold, while rendering small energy variations unresolvable far from the threshold [Fig. 2(a)]. Repulsive particle interactions may thereby enable the *selective* transmission of information about interaction energies close to the threshold. When suitably optimized, such an information bottleneck can pick up specific task-relevant features of the input [68–71]. By controlling the gain and threshold, the biophysical parameters \bar{d} and d_0 determine the amplified signal range, similar to the tunable resistors that shape the nonlinear mapping between input and output voltages in electronic audio processing [72].

To investigate how these parameters influence the compression of the original input, we first analyze the channel noise arising due to the microscopic particle dynamics. Discretizing space into boxes indexed by $j = 1, 2, \dots, B$ allows representing the particle and energy fields as random vectors which take realizations $\{\rho_j\}$ and $\{\epsilon_j\}$ from a finite set of density values S_ρ and energy states S_ϵ . Considering the limit of large particle numbers in a coarse-graining area element a , we approximate the conditional probability $P(\rho_j|\{\epsilon_k\})$ of a realization ρ_j given a set of binding energies by a Gaussian distribution with mean $\bar{\rho}_j(\{\epsilon_k\}) = \rho(\epsilon_j, l(\{\epsilon_k\}))$ given by Eq. (6), and standard deviation $\sigma_\rho(\bar{\rho}_j(\{\epsilon_k\})) = \sqrt{(1 - d_0^2 \bar{\rho}_j(\{\epsilon_k\})) \bar{\rho}_j(\{\epsilon_k\}) / a}$, such that the probability is conditioned on a realization of the entire binding energy vector through the parameter l [73, Supplementary Materials Sec. C1]. Metropolis-Hastings sampling of particle distributions numerically confirm these results [74, Supplementary Materials Fig. S1 and Sec. C1a].

To evaluate the level of selective signal amplification by the particle interactions, we compute the mutual information between the random vectors $\{\rho_j\}$ and $\{\epsilon_k\}$, given by

$$I = \sum_{\{\epsilon_k\}} \sum_{\{\rho_j\}} P(\{\rho_j\}, \{\epsilon_k\}) \ln \frac{P(\{\rho_j\}, \{\epsilon_k\})}{P(\{\rho_j\})P(\{\epsilon_k\})}, \quad (9)$$

in which the sums run over all possible realizations of the input and output sequences [107, Chapter 2, Supplementary Materials Sec. C2]. The joint probability $P(\{\rho_j\}, \{\epsilon_k\})$ is the product of the conditional probability $P(\{\rho_j\}|\{\epsilon_k\}) = \prod_j P(\rho_j|\{\epsilon_k\})$ —where $P(\rho_j|\{\epsilon_k\})$ is approximated as discussed above—and the probability of the input energy vector $P(\{\epsilon_k\})$. The distribution $P(\{\epsilon_k\})$ takes a system-specific form, depending on the statistics of binding energy variations across different environments. We consider in the following that $P(\{\epsilon_k\}) = \prod_k P(\epsilon_k)$ with the local values ϵ_k being independent uniform variates over S_ϵ , i.e. $P(\epsilon_k) = 1/|S_\epsilon|$, where $\epsilon_{\min} = \inf S_\epsilon = \epsilon_c$ corresponds to the most favorable possible energy level, and the maximum interaction energy $\epsilon_{\max} = \sup S_\epsilon$ corresponds to the least favorable input state.

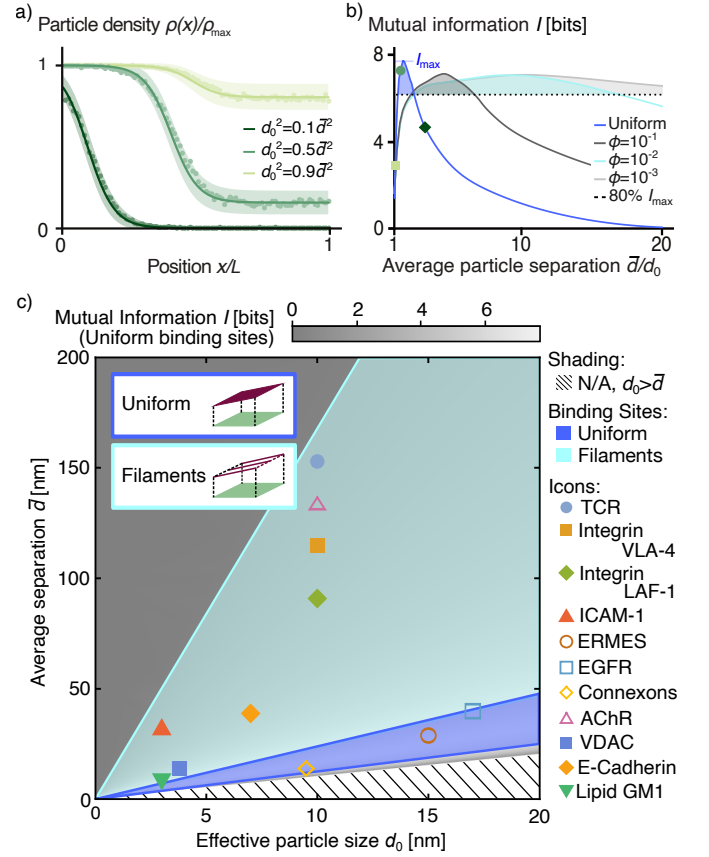


FIG. 2. Repulsive particle interactions threshold binding energy profiles. a) Sigmoidal equilibrium density fields form in response to a nonuniform particle-environment interaction energy $\epsilon(x) = k_B T(20x/L - 10)$ on a domain of length L (points from Metropolis-Hastings sampling [Supplementary Materials Sec. C1a], shading denotes two standard deviations). b) The mutual information between the external field and the particle density profile shows a maximum as a function of \bar{d}/d_0 , where the gain is high and the threshold energy is kept within the input range (computed for a system discretized as described in [Supplementary Materials Sec. C2]). The optimal information transmission regime—in which I is within 80% of its maximum—becomes larger as the area fraction ϕ of non-uniform binding sites along parallel lines is decreased. Icons label parameter values used in (a). c) The optimal information transmission regime is much larger for an actin-like area fraction $\phi = 10^{-2}$ [75, Supplementary Materials Sec. D] (light blue) than for uniform 2D sheets (dark blue). Macromolecular complexes in cells (colored icons, values from [76–106, Supplementary Materials Tab. S1]) indeed often associate with filamentous structures, such as the actin cytoskeleton (e.g. AChR, E-Cadherin).

Numerical evaluation of Eq.(9) for a range of parameter values reveals an optimal regime of particle-mediated physical thresholding [Fig. 2(b),ZSupplementary Materials Sec. C2]. Filters within this regime have threshold energies within the input range (i.e. $\epsilon_{\min} < \epsilon_{\text{th}} < \epsilon_{\max}$) and gains large enough to overcome the channel noise.

This optimal regime depends on the spatial organi-

zation of interaction sites, which in biological systems are often irregular. While for uniform binding-site densities below the maximum particle density, the maximum transmitted information is reduced [Supplementary Materials Fig. S2], some nonuniform binding-site distributions can increase information transmission, and extend the optimal regime to a broader range of parameters. To identify, in particular, how information transmission is influenced when particles bind to structures such as cytoskeletal filaments, we consider binding sites confined to parallel lines that cover a fraction ϕ of the total membrane surface [Supplementary Materials Sec. C3] [108]. We find that lowering ϕ allows effective information transfer with fewer particles in the 2D membrane compared to the case of uniform binding sites [Fig. 2(b)]. In cellular contexts, protein *line*-densities associated with such quasi-1D structures indeed influence many subcellular processes such as the generation of tension by motor proteins along filaments, or molecular events at cell-cell contact lines [109–113].

These optimal parameter regions for information transmission raise the question where the real surface-associated protein complexes and other macromolecular structures in biological cells fall. Bioimaging technologies are starting to overcome the challenges associated with visualizing nm-scale spatial arrangements of proteins along interfaces [114, 115], and, in some cases, effective particle sizes and typical cellular concentrations have been reported or can be inferred from other measurements [Supplementary Materials Tab. S1]. Indeed, we find that proteins known to associate with actin fibers or bundles (AChR [116–118], E-Cadherin [119], TCR [120], ICAM-1 [121, 122]) fall within the region in which information transmission from filamentous networks with an actin-like area fraction is optimal, whereas some proteins known to bind between neighboring cell membranes (connexons [123, 124]) or subcellular membraneous structures (ERMES [92, 125]) have sizes and surface densities that position them where information transmission is highest for uniform interaction sites [Fig. 2(c), Supplementary Materials Sec. D].

Physical thresholding at the nuclear envelope.—For large macromolecular structures, only a relatively small number of particles is required to form extended maximum-density regions. As a specific experimental example, we focus on nuclear pore complexes (NPCs) [126]. These protein complexes, approximately 100 nm in diameter, are embedded within the nuclear envelope—an intracellular membrane that forms the physical and regulatory interface between the cytoplasm and the nuclear interior [127, 128]. In addition to controlling nucleocytoplasmic transport, NPCs interact with the extranuclear cytoskeleton to regulate intranuclear states, including gene expression [129–132]. Yet how the spatial distribution of NPCs influences information transfer between cellular and nuclear states remains unclear [133–138].

We measure how nuclear pore complex distributions re-

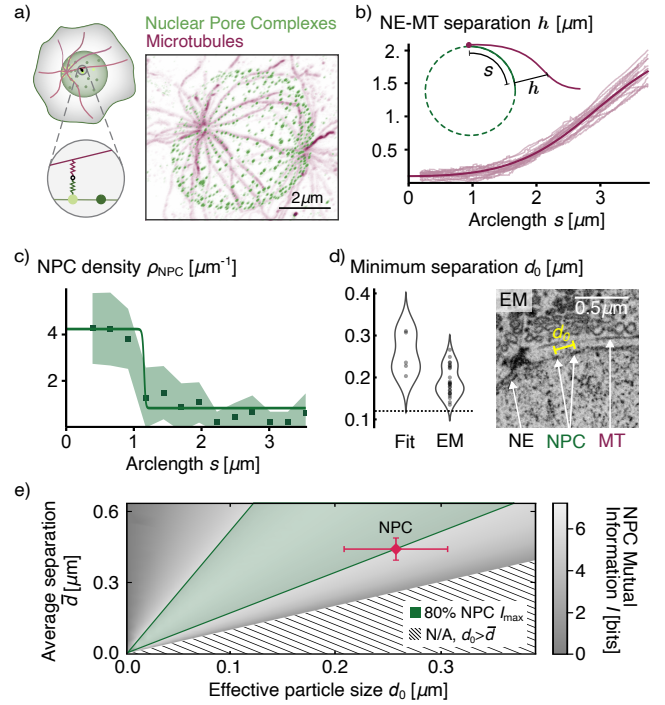


FIG. 3. Nuclear pore complexes (NPCs) form sigmoidal line-densities along extranuclear microtubule filaments in *S. arctica* nuclei. a) Ultrastructure expansion microscopy shows the spatial organisation of immunofluorescently labelled microtubules (purple) and NPCs (green) on an *S. arctica* nucleus (maximum intensity projection) [Supplementary Materials Sec. E1b]. b) The shortest separation distance between the nuclear envelope (NE) and the microtubule (MT) filaments increases as a function of the arc length s away from the microtubule organizing center at the pole. Light purple: individual tracks for one of five clusters. Dark purple: rational-exponential reparameterization of these tracks [Supplementary Materials Sec. E2a]. c) Fitting (solid line) the measured NPC line-density (dots) for the MT cluster in (b) with Eq. (6) yields parameter estimates for the effective spring constant λ and for the minimum NPC separation distance d_0 [Supplementary Materials Tab. S3]. Shaded area: 95% confidence interval. Other fitted profiles shown in [Supplementary Materials Fig. S3]. d) Left: Fit values for the minimum NPC separation d_0 compare well with independent measurements of d_0 from electron microscopy (EM) imaging, dashed line denotes the diameter of the complex 120 nm. Right: an example EM image with labeled features. e) The fitted d_0 value, and the average NPC separation distance \bar{d} measured from the data, indicate that NPC distributions can efficiently threshold microtubule proximity, given the measured filament density in this system $\phi = 0.21 \pm 0.03$.

spond to different configurations of the extranuclear microtubule cytoskeleton using expansion microscopy and immunostaining of *S. arctica* nuclei [Fig. 3(a), Supplementary Materials Fig. S3 and Sec. E, [139]] [60, 140]. Quantifying the separation distance between individual microtubule filaments and the nuclear surface reveals increasing height profiles from their anchor point at the

pole towards the nucleus equator [Fig. 3(b)]. We estimate the NPC density profiles along the filament arc length by taking averages across clusters of similar filaments and fitting Eq. (6) to this data, assuming that the effective binding energy profiles arise from the combination of a fixed interaction energy and an effective Hookean elastic contribution, as in Eq. (4) [Fig. 3(c), Supplementary Materials Fig. S3][141]. This assumption implies that heterogeneities in the interactions between NPCs and microtubules arise in this system primarily due to differences in the proximity of filaments to the nuclear envelope. We thereby obtain estimates for the effective NPC size $d_{0,\text{NPC}} = (260 \pm 50) \text{ nm}$, and the spring constant characterizing the elastic interaction between NPCs and microtubule filaments $\lambda_{\text{NPC}} = (0.04 \pm 0.03) \text{ pN nm}^{-1}$ [Supplementary Materials Tab. S3]. Our estimates of the minimal NPC separation distance—which we further corroborated using focused ion beam-scanning electron microscopy imaging—are larger than their diameter, suggesting additional non-steric repulsion effects, for example due to curvature-mediated interactions arising from nuclear-envelope deformations close to the NPCs [Fig. 3(d)] [60, 142, Supplementary Materials Sec. E2 and Tab. S2].

Computing the transmitted information given a surface area fraction corresponding to that of the MT filaments at the nuclear envelope in this system ($\phi = 0.21$) reveals that their effective size and total number allows these NPCs to efficiently threshold the MT proximity profiles [Fig. 3(e), Supplementary Materials Sec. C3].

Together, these results suggest that NPCs form sigmoidal density profiles along microtubule filaments due to their large effective size and fixed number [60, 143–146]. We propose that the thresholded readout of filament proximity could coordinate intranuclear functions, consistent with observations that microtubule–nucleus interactions influence e.g. chromatin organisation, gene expression, and mitotic remodelling [59, 60, 147–152].

Conclusions and outlook—In summary, we find that simple physical interactions at the interfaces of membrane-enclosed cellular compartments lead to the selective transmission of information, permitting the binary classification of surface regions. In particular, we report that short-range repulsion between membrane-embedded particles, such as arising from shielded electrostatic repulsion [153] or membrane-mediated interactions [50, 154, 155], produces a sigmoidal mapping between non-uniform external energies and the particle densities that form in response. We show how the nonlinear amplification of environmental heterogeneities is controlled by the effective interaction range of the particles and their total

number relative to the surface size, and we identify a regime of optimal information transmission for this physical thresholding, as determined by the gain and threshold of the sigmoid. Indeed, many surface-associated subcellular structures fall within the optimal regime based on their sizes and typical cellular concentrations, and our own measurements of *S. arctica* nuclear pore complex distributions reveal sigmoidal density profiles associated with extranuclear microtubule filaments. Interestingly, membrane-associated proteins often interact with irregularly shaped structures such as filamentous networks leading to quasi-1D interactions that facilitate the capacity for physical thresholding [156, 157]. How coupling between structures of different effective dimensions influences biological processes and functions has also been investigated in the context of chemical reaction networks [158, 159] and macromolecular assembly [160].

Sigmoidal filters are used in controlling thermostats, photoresistor circuits, bandpass filters, and neural networks, e.g. to introduce nonlinearities, and to threshold outputs. It will be interesting to investigate how sigmoidal particle distributions interact with downstream cellular processes, aiding pattern recognition-like functions of compartment surfaces. The selective transmission of information at the cell surface could guide for example directed movements in response to external gradients in mechanical or chemical properties.

Analyzing other types of particle interactions could reveal whether more complex transformations are possible that would permit operations such as edge detection or object recognition. We anticipate that our increasing technical ability to measure molecular patterns in cells at the sub- μm scale will enable the discovery of new physical information processing modalities through which cells and subcellular structures perceive their complex surroundings.

Acknowledgments

Acknowledgements.—We thank Tim Dullweber, Ian Estabrook, Pamela Guruciaga, Patrick Jentsch, Johannes Jung, Thomas Quail, Jan Rombouts, Sacha Sokoloski, and Laeschkir Würthner for useful discussions and feedback on the manuscript, and Omayya Dudin for his advice and expertise. All authors acknowledge funding from the EMBL. H.S. was supported by the EMBL Interdisciplinary Postdoctoral Fellowship (EIPD4) programme under Marie Skłodowska-Curie Actions Cofund (grant agreement no. 847543). G.D. and H.S. are supported by the European Union (ERC, KaryodynEvo, 101078291).

[1] K. P. Adamala, M. Dogterom, Y. Elani, P. Schwille, M. Takinoue, and T.-Y. D. Tang, Present and future of

synthetic cell development, *Nature Reviews Molecular Cell Biology* **25**, 162 (2024).

- [2] C. E. Shannon, Von Neumann’s contributions to automata theory, *Bulletin of the American Mathematical Society* **64**, 123 (1958).
- [3] K. D. Farnsworth, J. Nelson, and C. Gershenson, Living is Information Processing: From Molecules to Global Systems, *Acta Biotheoretica* **61**, 203 (2013).
- [4] I. R. Graf and B. B. Machta, A bifurcation integrates information from many noisy ion channels and allows for milli-kelvin thermal sensitivity in the snake pit organ, *Proceedings of the National Academy of Sciences* **121**, e2308215121 (2024).
- [5] T. Dullweber and A. Erzberger, Mechanochemical feedback loops in contact-dependent fate patterning, *Current Opinion in Systems Biology* **32-33**, 100445 (2023).
- [6] S. Uda, Application of information theory in systems biology, *Biophysical Reviews* **12**, 377 (2020).
- [7] J. Estrada, F. Wong, A. DePace, and J. Gunawardena, Information Integration and Energy Expenditure in Gene Regulation, *Cell* **166**, 234 (2016).
- [8] C. Collinet and T. Lecuit, Programmed and self-organized flow of information during morphogenesis, *Nature Reviews Molecular Cell Biology* **22**, 245 (2021).
- [9] A. Ganesan and J. Zhang, How cells process information: Quantification of spatiotemporal signaling dynamics, *Protein Science : A Publication of the Protein Society* **21**, 918 (2012).
- [10] R. Cheong, A. Rhee, C. J. Wang, I. Nemenman, and A. Levchenko, Information Transduction Capacity of Noisy Biochemical Signaling Networks, *Science* **334**, 354 (2011).
- [11] M. D. Brennan, R. Cheong, and A. Levchenko, How Information Theory Handles Cell Signaling and Uncertainty, *Science* **338**, 334 (2012).
- [12] M. Kramar, L. Hahn, A. M. Walczak, T. Mora, and M. Coppey, [arXiv:2410.22571 \[q-bio.CB\]](https://arxiv.org/abs/2410.22571).
- [13] A. Nandan, A. Das, R. Lott, and A. Koseska, Cells use molecular working memory to navigate in changing chemoattractant fields, *eLife* **11**, e76825 (2022).
- [14] G. Falasco, R. Rao, and M. Esposito, Information Thermodynamics of Turing Patterns, *Physical Review Letters* **121**, 108301 (2018).
- [15] F. Avanzini, T. Aslyamov, E. Fodor, and M. Esposito, Nonequilibrium thermodynamics of non-ideal reaction–diffusion systems: Implications for active self-organization, *The Journal of Chemical Physics* **161**, 174108 (2024).
- [16] D. B. Brückner and G. Tkačik, Information content and optimization of self-organized developmental systems, *Proceedings of the National Academy of Sciences* **121**, e2322326121 (2024).
- [17] L. Wolpert, Positional information and pattern formation in development, *Developmental Genetics* **15**, 485 (1994).
- [18] J. O. Dubuis, G. Tkačik, E. F. Wieschaus, T. Gregor, and W. Bialek, Positional information, in bits, *Proceedings of the National Academy of Sciences* **110**, 16301 (2013).
- [19] G. Tkačik and T. Gregor, The many bits of positional information, *Development* **148**, dev176065 (2021).
- [20] L. McGough, H. Casademunt, M. Nikolić, Z. Aridor, M. D. Petkova, T. Gregor, and W. Bialek, Finding the Last Bits of Positional Information, *PRX Life* **2**, 013016 (2024).
- [21] G. P. Flowers and C. M. Crews, Remembering where we are: Positional information in salamander limb regeneration, *Developmental Dynamics* **249**, 465 (2020).
- [22] K. Zieske and P. Schwill, Reconstitution of self-organizing protein gradients as spatial cues in cell-free systems, *eLife* **3**, e03949 (2014).
- [23] M. C. Wigbers, T. H. Tan, F. Brauns, J. Liu, S. Z. Swartz, E. Frey, and N. Fakhri, A hierarchy of protein patterns robustly decodes cell shape information, *Nature Physics* **17**, 578 (2021).
- [24] L. Wettmann and K. Kruse, The Min-protein oscillations in Escherichia coli: an example of self-organized cellular protein waves, *Philosophical Transactions of the Royal Society B: Biological Sciences* **373**, 20170111 (2018).
- [25] A. Haupt and N. Minc, How cells sense their own shape – mechanisms to probe cell geometry and their implications in cellular organization and function, *Journal of Cell Science* **131**, jcs214015 (2018).
- [26] P. Rangamani, A. Lipshtat, E. U. Azeloglu, R. C. Calizo, M. Hu, S. Ghassemi, J. Hone, S. Scarlata, S. R. Neves, and R. Iyengar, Decoding information in cell shape, *Cell* **154**, 1356 (2013).
- [27] C. G. Evans, J. O’Brien, E. Winfree, and A. Murugan, Pattern recognition in the nucleation kinetics of nonequilibrium self-assembly, *Nature* **625**, 500 (2024).
- [28] T. Mijatović, A. R. Kok, J. W. Zwanikken, and M. Bauer, [arXiv:2505.07641 \[physics.bio-ph\]](https://arxiv.org/abs/2505.07641).
- [29] R. Braz Teixeira, G. Carugno, I. Neri, and P. Sartori, Liquid hopfield model: Retrieval and localization in multicomponent liquid mixtures, *Proceedings of the National Academy of Sciences* **121**, e2320504121 (2024).
- [30] D. S. Banerjee, M. J. Falk, M. L. Gardel, A. M. Walczak, T. Mora, and S. Vaikuntanathan, [arXiv:2504.15107 \[cond-mat.soft\]](https://arxiv.org/abs/2504.15107).
- [31] J. Rombouts, J. Elliott, and A. Erzberger, Forceful patterning: theoretical principles of mechanochemical pattern formation, *EMBO reports* **24**, e57739 (2023).
- [32] E. Sitarska, S. D. Almeida, M. S. Beckwith, J. Stopp, J. Czuchnowski, M. Siggel, R. Roessner, A. Tschanz, C. Ejsing, Y. Schwab, J. Kosinski, M. Sixt, A. Kreshuk, A. Erzberger, and A. Diz-Muñoz, Sensing their plasma membrane curvature allows migrating cells to circumvent obstacles, *Nature Communications* **14**, 5644 (2023).
- [33] E. R. Gomes, S. Jani, and G. G. Gundersen, Nuclear movement regulated by cdc42, mrck, myosin, and actin flow establishes mtoc polarization in migrating cells, *Cell* **121**, 451 (2005).
- [34] E. Vercruysse, D. B. Brückner, M. Gómez-González, A. Remson, M. Luciano, Y. Kalukula, L. Rossetti, X. Trepas, E. Hannezo, and S. Gabriele, Geometry-driven migration efficiency of autonomous epithelial cell clusters, *Nature Physics* **20**, 1492 (2024).
- [35] J. d’Alessandro, A. Barbier-Chebbah, V. Cellierin, O. Benichou, R. M. Mège, R. Voituriez, and B. Ladoux, Cell migration guided by long-lived spatial memory, *Nature Communications* **12**, 4118 (2021).
- [36] J. E. Ron, M. Crestani, J. M. Kux, J. Liu, N. Al-Dam, P. Monzo, N. C. Gauthier, P. J. Sáez, and N. S. Gov, Emergent seesaw oscillations during cellular directional decision-making, *Nature Physics* **20**, 501 (2024).
- [37] Y. Han, X. Liu, S. Qu, X. Duan, Y. Xiang, N. Jiang, S. Yang, X. Fang, L. Xu, H. Wen, Y. Yu, S. Huang, J. Huang, and K. Zhu, Tissue geometry spatiotempo-

- rally drives bacterial infections, *Cell* (2025), (to be published).
- [38] M. V. Baranov, M. Kumar, S. Sacanna, S. Thutupalli, and G. van den Bogaart, Modulation of immune responses by particle size and shape, *Frontiers in Immunology* **11**, 607945 (2021).
 - [39] J. L. Stow and N. D. Condon, The cell surface environment for pathogen recognition and entry, *Clinical & Translational Immunology* **5**, e71 (2016).
 - [40] S. Cho, J. Irianto, and D. E. Discher, Mechanosensing by the nucleus: From pathways to scaling relationships, *Journal of Cell Biology* **216**, 305 (2017).
 - [41] T. Burkart, M. C. Wigbers, L. Würthner, and E. Frey, Control of protein-based pattern formation via guiding cues, *Nature Reviews Physics* **4**, 511 (2022).
 - [42] A. Shellard and R. Mayor, All roads lead to directional cell migration, *Trends in Cell Biology* **30**, 852 (2020).
 - [43] A. G. Clark, A. Maitra, C. Jacques, M. Bergert, C. Pérez-González, A. Simon, L. Lederer, A. Diz-Muñoz, X. Trepát, R. Voituriez, and D. M. Vignjevic, Self-generated gradients steer collective migration on viscoelastic collagen networks, *Nature Materials* **21**, 1200 (2022).
 - [44] S. B. Carter, Haptotaxis and the mechanism of cell motility, *Nature* **213**, 256 (1967).
 - [45] X. Luo, V. Seveau de Noray, L. Aoun, M. Biarnes-Pelicot, P.-O. Strale, V. Studer, M.-P. Valignat, and O. Theodoly, Lymphocytes perform reverse adhesive haptotaxis mediated by lfa-1 integrins, *Journal of Cell Science* **133**, jcs242883 (2020).
 - [46] I. C. Fortunato, D. B. Brückner, S. Grosser, L. Rossetti, M. Bosch-Padrós, J. Trebicka, P. Roca-Cusachs, R. Sunyer, E. Hannezo, and X. Trepát, Single cell migration along and against confined haptotactic gradients, *bioRxiv* [10.1101/2024.12.02.626413](https://doi.org/10.1101/2024.12.02.626413) (2024).
 - [47] R. J. Leiphart, D. Chen, A. P. Peredo, A. E. Loneker, and P. A. Janmey, Mechanosensing at cellular interfaces, *Langmuir* **35**, 7509 (2019).
 - [48] C. Ji and Y. Huang, Durotaxis and negative durotaxis: where should cells go?, *Communications Biology* **6**, 1169 (2023).
 - [49] W.-J. Rappel and L. Edelstein-Keshet, Mechanisms of cell polarization, *Current Opinion in Systems Biology* **3**, 43 (2017).
 - [50] C. Yolcu, R. C. Haussman, and M. Deserno, The effective field theory approach towards membrane-mediated interactions between particles, *Advances in Colloid and Interface Science* **208**, 89 (2014).
 - [51] M. A. S. Karal, M. M. Billah, M. Ahmed, and M. K. Ahamed, A review on the measurement of the bending rigidity of lipid membranes, *Soft Matter* **19**, 8285 (2023).
 - [52] R. L. Liboff, Transport coefficients determined using the shielded coulomb potential, *The Physics of Fluids* **2**, 40 (1959).
 - [53] J. Rowlinson, The yukawa potential, *Physica A: Statistical Mechanics and its Applications* **156**, 15 (1989).
 - [54] R. Milo and R. Phillips, Cell biology by the numbers (Garland Science, New York, 2015) Chap. 1.
 - [55] V. P. Zhdanov, Conditions of appreciable influence of microrna on a large number of target mrnas, *Molecular BioSystems* **5**, 638 (2009).
 - [56] M. Hu, J. J. Briguglio, and M. Deserno, Determining the gaussian curvature modulus of lipid membranes in simulations, *Biophysical Journal* **102**, 1403 (2012).
 - [57] H. Wennerström, E. Vallina Estrada, J. Danielsson, and M. Oliveberg, Colloidal stability of the living cell, *Proceedings of the National Academy of Sciences* **117**, 10113 (2020).
 - [58] R. Seelaboyina and R. Vishwakarma, Different thresholding techniques in image processing : A review, in *ICDSMLA 2021*, edited by A. Kumar, S. Senatore, and V. K. Gunjan (Springer Nature Singapore, Singapore, 2023) pp. 23–29.
 - [59] O. Dudin, A. Ondracka, X. Grau-Bové, A. A. Haraldsen, A. Toyoda, H. Suga, J. Bråte, and I. Ruiz-Trillo, A unicellular relative of animals generates a layer of polarized cells by actomyosin-dependent cellularization, *eLife* **8**, e49801 (2019).
 - [60] H. Shah, M. Olivetta, C. Bhickta, P. Ronchi, M. Trupinić, E. C. Tromer, I. M. Tolić, Y. Schwab, O. Dudin, and G. Dey, Life-cycle-coupled evolution of mitosis in close relatives of animals, *Nature* **630**, 116 (2024).
 - [61] J. Halatek and E. Frey, Rethinking pattern formation in reaction–diffusion systems, *Nature Physics* **14**, 507 (2018).
 - [62] F. Brauns, J. Halatek, and E. Frey, Phase-space geometry of mass-conserving reaction-diffusion dynamics, *Physical Review X* **10**, 041036 (2020).
 - [63] C. W. Gardiner, Stochastic methods: A handbook for the natural and social sciences (Springer, Berlin, 2010) Chap. 13.
 - [64] R. Belousov, A. Hassanali, and É. Roldán, Statistical physics of inhomogeneous transport: Unification of diffusion laws and inference from first-passage statistics, *Physical Review E* **106**, 014103 (2022).
 - [65] A. H. Carter, *Classical and statistical thermodynamics* (Pearson Education, Philadelphia, 2000).
 - [66] L. D. Landau and E. M. Lifshitz, Statistical physics (Butterworth-Heinemann, Oxford, 1996) p. 134, 3rd ed.
 - [67] T. L. Hill, An introduction to statistical thermodynamics (Dover Publications, Mineola, 1987) p. 128.
 - [68] N. Tishby, F. C. Pereira, and W. Bialek, [arXiv:physics/0004057 \[physics.data-an\]](https://arxiv.org/abs/physics/0004057).
 - [69] M. Bauer and W. Bialek, Information bottleneck in molecular sensing, *PRX Life* **1**, 023005 (2023).
 - [70] M. Bauer, How does an organism extract relevant information from transcription factor concentrations?, *Biochemical Society Transactions* **50**, 1365 (2022).
 - [71] M. Kleinman, T. Wang, D. Xiao, E. Fegghi, K. Lee, N. Carr, Y. Li, N. Hadidi, C. Chandrasekaran, and J. C. Kao, The information bottleneck as a principle underlying multi-area cortical representations during decision-making, *bioRxiv* [10.1101/2023.07.12.548742](https://doi.org/10.1101/2023.07.12.548742) (2025).
 - [72] R. Mancini, Chapter 6 - development of the non ideal op amp equations, in *Op Amps for Everyone (Second Edition)*, edited by R. Mancini (Newnes, Burlington, 2003) second edition ed., pp. 67–75.
 - [73] H. Touchette, The large deviation approach to statistical mechanics, *Physics Reports* **478**, 1 (2009).
 - [74] J. Elliott, Elliott2025 metropolis simulations, <https://git.embl.de/elliott/Elliott2025-Metropolis-Simulations> (2025).
 - [75] S. Lembo, L. Strauss, D. Cheng, J. Vermeil, M. Siggel, M. Toro-Nahuelpan, C. J. Chan, J. Kosinski, M. Piel, O. Du Roure, J. Heuvingh, J. Mahamid, and A. Diz-Muñoz, The distance between the

- plasma membrane and the actomyosin cortex acts as a nanogate to control cell surface mechanics, *bioRxiv* [10.1101/2023.01.31.526409](https://doi.org/10.1101/2023.01.31.526409) (2023).
- [76] P. Robert, M. Biarnes-Pelicot, N. Garcia-Seyda, P. Hatoum, D. Touchard, S. Brustlein, P. Nicolas, B. Malissen, M.-P. Valignat, and O. Theodoly, Functional mapping of adhesiveness on live cells reveals how guidance phenotypes can emerge from complex spatiotemporal integrin regulation, *Frontiers in Bioengineering and Biotechnology* **9**, 625366 (2021).
- [77] B. L. Ekerdt, R. A. Segalman, and D. V. Schaffer, Spatial organization of cell-adhesive ligands for advanced cell culture, *Biotechnology Journal* **8**, 1411 (2013).
- [78] B.-A. Truong Quang, M. Mani, O. Markova, T. Lecuit, and P.-F. Lenne, Principles of e-cadherin supramolecular organization in vivo, *Current Biology* **23**, 2197 (2013).
- [79] C. A. Janeway Jr., P. Travers, M. Walport, and et al., in *Immunobiology: The Immune System in Health and Disease* (Garland Science, New York, 2001) Chap. Antigen recognition by T cells, 5th ed.
- [80] X. Jiang, S. Dudzinski, K. E. Beckermann, K. Young, E. McKinley, J. O. McIntyre, J. C. Rathmell, J. Xu, and J. C. Gore, Mri of tumor t cell infiltration in response to checkpoint inhibitor therapy, *Journal for Immunotherapy of Cancer* **8**, e000328 (2020).
- [81] M. Swamy, E. P. Dopfer, E. Molnar, B. Alarcón, and W. W. A. Schamel, The 450kda tcr complex has a stoichiometry of $\alpha\beta\gamma\delta\epsilon\zeta$, *Scandinavian Journal of Immunology* **67**, 418 (2008).
- [82] V. P.-Y. Ma, Y. Hu, A. V. Kellner, J. M. Brockman, A. Velusamy, A. T. Blanchard, B. D. Evavold, R. Alon, and K. Salaita, The magnitude of lfa-1/icam-1 forces fine-tune tcr-triggered t cell activation, *Science Advances* **8**, eabg4485 (2022).
- [83] T. M. Bui, H. L. Wiesolek, and R. Sumagin, Icam-1: A master regulator of cellular responses in inflammation, injury resolution, and tumorigenesis, *Journal of Leukocyte Biology* **108**, 787 (2020).
- [84] G. Kurz-Isler, T. Voigt, and H. Wolburg, Modulation of connexon densities in gap junctions of horizontal cell perikarya and axon terminals in fish retina: effects of light/dark cycles, interruption of the optic nerve and application of dopamine, *Cell & Tissue Research* **268**, 267 (1992).
- [85] D. A. Goodenough and J. P. Revel, A fine structural analysis of intercellular junctions in the mouse liver, *The Journal of Cell Biology* **45**, 272 (1970).
- [86] A. Kuntze, O. Goetsch, B. Fels, K. Najder, A. Unger, M. Wilhelmi, S. Sargin, S. Schimmelpfennig, I. Neumann, A. Schwab, and Z. Pethő, Protonation of piezo1 impairs cell-matrix interactions of pancreatic stellate cells, *Frontiers in Physiology* **11**, 89 (2020).
- [87] E. M. Mulhall, A. Gharpure, R. M. Lee, A. E. Dubin, J. S. Aaron, K. L. Marshall, K. R. Spencer, M. A. Reiche, S. C. Henderson, T.-L. Chew, and A. Patapoutian, Direct observation of the conformational states of piezo1, *Nature* **620**, 1117 (2023).
- [88] V. Rizzo, C. Morton, N. DePaola, J. E. Schnitzer, and P. F. Davies, Recruitment of endothelial caveolae into mechanotransduction pathways by flow conditioning in vitro, *American Journal of Physiology-Heart and Circulatory Physiology* **285**, H1720 (2003).
- [89] P. Thomsen, K. Roepstorff, M. Stahlhut, and B. van Deurs, Caveolae are highly immobile plasma membrane microdomains, which are not involved in constitutive endocytic trafficking, *Molecular Biology of the Cell* **13**, 238 (2002).
- [90] C. A. Mannella, Vdac—a primal perspective, *International Journal of Molecular Sciences* **22**, 1685 (2021).
- [91] S. Hiller, J. Abramson, C. Mannella, G. Wagner, and K. Zeth, The 3d structures of vdac represent a native conformation, *Trends in Biochemical Sciences* **35**, 514 (2010).
- [92] M. R. Wozny, A. Di Luca, D. R. Morado, A. Picco, R. Khaddaj, P. Campomanes, L. Ivanović, P. C. Hoffmann, E. A. Miller, S. Vanni, and W. Kukulski, In situ architecture of the er-mitochondria encounter structure, *Nature* **618**, 188 (2023).
- [93] Y. Lyu, S. Chen, Y. Zhao, H. Yuan, C. Zhang, C. Zhang, and Q. Meng, Effect of gm1 concentration change on plasma membrane: molecular dynamics simulation and analysis, *Physical Chemistry Chemical Physics* **26**, 12552 (2024).
- [94] E. H. Mojumdar, C. Grey, and E. Sparr, Self-assembly in ganglioside-phospholipid systems: The co-existence of vesicles, micelles, and discs, *International Journal of Molecular Sciences* **21**, 56 (2020).
- [95] S. Evans, D. Goldman, S. Heinemann, and J. Patrick, Muscle acetylcholine receptor biosynthesis. regulation by transcript availability., *Journal of Biological Chemistry* **262**, 4911 (1987).
- [96] D. K. McMahon, P. A. Anderson, R. Nassar, J. B. Bunting, Z. Saba, A. E. Oakeley, and N. N. Malouf, C2c12 cells: biophysical, biochemical, and immunocytochemical properties, *American Journal of Physiology-Cell Physiology* **266**, C1795 (1994).
- [97] M. M. S. Lo, E. A. Barnard, and J. O. Dolly, Size of acetylcholine receptors in the membrane. an improved version of the radiation inactivation method, *Biochemistry* **21**, 2210 (1982).
- [98] L. Geng, H. L. Zhang, and H. B. Peng, The formation of acetylcholine receptor clusters visualized with quantum dots, *BMC Neuroscience* **10**, 80 (2009).
- [99] C. Kerntke, F. Nimmerjahn, and M. Biburger, There is (scientific) strength in numbers: A comprehensive quantitation of fc gamma receptor numbers on human and murine peripheral blood leukocytes, *Frontiers in Immunology* **11**, 118 (2020).
- [100] V. Wacleche, C. Tremblay, J.-P. Routy, and P. Ancuta, The biology of monocytes and dendritic cells: Contribution to hiv pathogenesis, *Viruses* **10**, 65 (2018).
- [101] F. Saji, Dynamics of immunoglobulins at the fetomaternal interface, *Reviews of Reproduction* **4**, 81 (1999), bNID 117058.
- [102] F. Zhang, S. Wang, L. Yin, Y. Yang, Y. Guan, W. Wang, H. Xu, and N. Tao, Quantification of epidermal growth factor receptor expression level and binding kinetics on cell surfaces by surface plasmon resonance imaging, *Analytical Chemistry* **87**, 9960 (2015).
- [103] A. Abulrob, Z. Lu, E. Baumann, D. Vobornik, R. Taylor, D. Stanimirovic, and L. J. Johnston, Nanoscale imaging of epidermal growth factor receptor clustering, *Journal of Biological Chemistry* **285**, 3145 (2010).
- [104] U. Horzum, B. Ozdil, and D. Pesen-Okvur, Step-by-step quantitative analysis of focal adhesions, *MethodsX* **1**, 56 (2014).
- [105] T. N. TruongVo, R. M. Kennedy, H. Chen, A. Chen,

- A. Berndt, M. Agarwal, L. Zhu, H. Nakshatri, J. Wallace, S. Na, H. Yokota, and J. E. Ryu, Microfluidic channel for characterizing normal and breast cancer cells, *Journal of Micromechanics and Microengineering* **27**, 035017 (2017).
- [106] H. P. Erickson, Size and shape of protein molecules at the nanometer level determined by sedimentation, gel filtration, and electron microscopy, *Biological Procedures Online* **11**, 32 (2009).
- [107] T.M. Cover and J. A. Thomas, *Elements of Information Theory*, 99th ed., Wiley Series in Telecommunications and Signal Processing (John Wiley & Sons, Nashville, 1991).
- [108] T. Hohmann and F. Dehghani, The cytoskeleton—a complex interacting meshwork, *Cells* **8**, 362 (2019).
- [109] Y. Cho, D. Haraguchi, K. Shigetomi, K. Matsuzawa, S. Uchida, and J. Ikenouchi, Tricellulin secures the epithelial barrier at tricellular junctions by interacting with actomyosin, *Journal of Cell Biology* **221**, e202009037 (2022).
- [110] M. Resnik-Docampo, C. L. Koehler, R. I. Clark, J. M. Schinaman, V. Sauer, D. M. Wong, S. Lewis, C. D’Alterio, D. W. Walker, and D. L. Jones, Tricellular junctions regulate intestinal stem cell behaviour to maintain homeostasis, *Nature Cell Biology* **19**, 52 (2017).
- [111] J. Howard, Mechanical signaling in networks of motor and cytoskeletal proteins, *Annual Review of Biophysics* **38**, 217 (2009).
- [112] X. Sun and G. M. Alushin, Cellular force-sensing through actin filaments, *The FEBS Journal* **290**, 2576 (2023).
- [113] F. Bosveld, O. Markova, B. Guirao, C. Martin, Z. Wang, A. Pierre, M. Balakireva, I. Gaugue, A. Ainslie, N. Christophorou, D. K. Lubensky, N. Minc, and Y. Bellaïche, Epithelial tricellular junctions act as interphase cell shape sensors to orient mitosis, *Nature* **530**, 495 (2016).
- [114] R. X. Norman, Y.-C. Chen, E. E. Recchia, J. Loi, Q. Rosemarie, S. L. Lesko, S. Patel, N. Sherer, M. Takaku, M. E. Burkard, and A. Suzuki, One step 4× and 12× 3d-exm enables robust super-resolution microscopy of nanoscale cellular structures, *Journal of Cell Biology* **224**, e202407116 (2025).
- [115] N. Radmacher, A. I. Chizhik, O. Nevskiy, J. I. Gallea, I. Gregor, and J. Enderlein, Molecular level super-resolution fluorescence imaging, *Annual Review of Biophysics* **54**, 163 (2025).
- [116] Z. Dai, X. Luo, H. Xie, and H. B. Peng, The actin-driven movement and formation of acetylcholine receptor clusters, *The Journal of Cell Biology* **150**, 1321 (2000).
- [117] Y. Chen, F. C. Ip, L. Shi, Z. Zhang, H. Tang, Y. P. Ng, W.-C. Ye, A. K. Fu, and N. Y. Ip, Coronin 6 regulates acetylcholine receptor clustering through modulating receptor anchorage to actin cytoskeleton, *The Journal of Neuroscience* **34**, 2413 (2014).
- [118] G. Xing, H. Jing, L. Zhang, Y. Cao, L. Li, K. Zhao, Z. Dong, W. Chen, H. Wang, R. Cao, W.-C. Xiong, and L. Mei, A mechanism in agrin signaling revealed by a prevalent rapsyn mutation in congenital myasthenic syndrome, *eLife* **8**, e49180 (2019).
- [119] R. B. Troyanovsky, I. Indra, and S. M. Troyanovsky, Actin-dependent α -catenin oligomerization contributes to adherens junction assembly, *Nature Communications* **16**, 1801 (2025).
- [120] M. L. Dustin and J. A. Cooper, The immunological synapse and the actin cytoskeleton: molecular hardware for t cell signaling, *Nature Immunology* **1**, 23 (2000).
- [121] L. Celli, J.-J. Ryckewaert, E. Delachanal, and A. Duperay, Evidence of a functional role for interaction between icam-1 and nonmuscle α -actinins in leukocyte diapedesis, *The Journal of Immunology* **177**, 4113 (2006).
- [122] O. Carpén, P. Pallai, D. E. Staunton, and T. A. Springer, Association of intercellular adhesion molecule-1 (icam-1) with actin-containing cytoskeleton and alpha-actinin., *The Journal of cell biology* **118**, 1223 (1992).
- [123] E. Y. Kirichenko, S. N. Skatchkov, and A. M. Ermakov, Structure and functions of gap junctions and their constituent connexins in the mammalian cns, *Biochemistry (Moscow), Supplement Series A: Membrane and Cell Biology* **15**, 107 (2021).
- [124] B. Alberts, D. Bray, J. Lewis, M. Raff, K. Roberts, and J. Watson, *Molecular Biology of the Cell* (Garland, New York, 2002) Chap. Cell Junctions, 4th ed.
- [125] J. Y. Cheema, J. He, W. Wei, and C. Fu, The endoplasmic reticulum-mitochondria encounter structure and its regulatory proteins, *Contact* **4**, 25152564211064491 (2021).
- [126] E. Dultz, M. Wojtynek, O. Medalia, and E. Onischenko, The Nuclear Pore Complex: Birth, Life, and Death of a Cellular Behemoth, *Cells* **11**, 1456 (2022).
- [127] S. Bahmanyar and C. Schlieker, Lipid and protein dynamics that shape nuclear envelope identity, *Molecular Biology of the Cell* **31**, 1315 (2020).
- [128] A. K. Balaji, S. Saha, S. Deshpande, D. Poola, and K. Sengupta, Nuclear envelope, chromatin organizers, histones, and dna: The many achilles heels exploited across cancers, *Frontiers in Cell and Developmental Biology* **10**, 1068347 (2022).
- [129] M. Soheilypour, M. Peyro, Z. Jahed, and M. R. K. Mofrad, On the nuclear pore complex and its roles in nucleo-cytoskeletal coupling and mechanobiology, *Cellular and Molecular Bioengineering* **9**, 217 (2016).
- [130] S. Biedzinski, G. Agsu, B. Vianay, M. Delord, L. Blanchoin, J. Larghero, L. Faivre, M. Théry, and S. Brunet, Microtubules control nuclear shape and gene expression during early stages of hematopoietic differentiation, *The EMBO Journal* **39**, e103957 (2020).
- [131] J. Geng, Z. Kang, Q. Sun, M. Zhang, P. Wang, Y. Li, J. Li, B. Su, and Q. Wei, Microtubule assists actomyosin to regulate cell nuclear mechanics and chromatin accessibility, *Research* **6**, 0054 (2023).
- [132] Y. Maizels and G. Gerlitz, Shaping of interphase chromosomes by the microtubule network, *The FEBS Journal* **282**, 3500 (2015).
- [133] A. Nair, J. Khanna, J. Kler, R. Ragesh, and K. Sengupta, Nuclear envelope and chromatin choreography direct cellular differentiation, *Nucleus* **16**, 2449520 (2025).
- [134] M. W. Goldberg, Nuclear pore complex tethers to the cytoskeleton, *Seminars in Cell & Developmental Biology* **68**, 52 (2017).
- [135] P. Huang, X. Zhang, Z. Cheng, X. Wang, Y. Miao, G. Huang, Y.-F. Fu, and X. Feng, The nuclear pore y-complex functions as a platform for transcriptional regulation of flowering locus c in arabidopsis, *The Plant Cell* **36**, 346 (2024).

- [136] Y. Guo and Y. Zheng, Lamins position the nuclear pores and centrosomes by modulating dynein, *Molecular Biology of the Cell* **26**, 3379 (2015).
- [137] L. M. Hoffman, M. A. Smith, C. C. Jensen, M. Yoshigi, E. Blankman, K. S. Ullman, and M. C. Beckerle, Mechanical stress triggers nuclear remodeling and the formation of transmembrane actin nuclear lines with associated nuclear pore complexes, *Molecular Biology of the Cell* **31**, 1774 (2020).
- [138] F. Donnaloja, E. Jacchetti, M. Soncini, and M. T. Raimondi, Mechanosensing at the nuclear envelope by nuclear pore complex stretch activation and its effect in physiology and pathology, *Frontiers in Physiology* **10**, 896 (2019).
- [139] J. Elliott, H. Shah, R. Belousov, G. Dey, and A. Erzberger, Image dataset used in 'Repulsive particle interactions enable selective information processing at cellular interfaces', <https://www.ebi.ac.uk/biostudies/bioimages/studies/S-BIAD2081> (2025).
- [140] J. Elliott, Elliott2025 image analysis s-arctica, <https://git.embl.de/elliott/Elliott2025-Image-Analysis-S-arctica> (2025).
- [141] L. Li, J. Alper, and E. Alexov, Cytoplasmic dynein binding, run length, and velocity are guided by long-range electrostatic interactions, *Scientific Reports* **6**, 31523 (2016).
- [142] J. Schindelin, I. Arganda-Carreras, E. Frise, V. Kaynig, M. Longair, T. Pietzsch, S. Preibisch, C. Rueden, S. Saalfeld, B. Schmid, J.-Y. Tinevez, D. J. White, V. Hartenstein, K. Eliceiri, P. Tomancak, and A. Cardona, Fiji: an open-source platform for biological-image analysis, *Nature Methods* **9**, 676 (2012).
- [143] N. Daigle, J. Beaudouin, L. Hartnell, G. Imreh, E. Hallberg, J. Lippincott-Schwartz, and J. Ellenberg, Nuclear pore complexes form immobile networks and have a very low turnover in live mammalian cells, *The Journal of Cell Biology* **154**, 71 (2001).
- [144] G. Rabut, V. Doye, and J. Ellenberg, Mapping the dynamic organization of the nuclear pore complex inside single living cells, *Nature Cell Biology* **6**, 1114 (2004).
- [145] B. H. Toyama and M. W. Hetzer, Protein homeostasis: live long, won't prosper, *Nature Reviews Molecular Cell Biology* **14**, 55 (2013).
- [146] J. M. Varberg, J. R. Unruh, A. J. Bestul, A. A. Khan, and S. L. Jaspersen, Quantitative analysis of nuclear pore complex organization in *Schizosaccharomyces pombe*, *Life Science Alliance* **5**, e202201423 (2022).
- [147] D. M. Roth, G. W. Moseley, D. Glover, C. W. Pouton, and D. A. Jans, A microtubule-facilitated nuclear import pathway for cancer regulatory proteins, *Traffic* **8**, 673 (2007).
- [148] D. M. Roth, G. W. Moseley, C. W. Pouton, and D. A. Jans, Mechanism of microtubule-facilitated "fast track" nuclear import, *Journal of Biological Chemistry* **286**, 14335 (2011).
- [149] M. E. Kelley, L. Carlini, N. Kornakov, A. Aher, A. Khodjakov, and T. M. Kapoor, Spastin regulates anaphase chromosome separation distance and microtubule-containing nuclear tunnels, *Molecular Biology of the Cell* **35**, ar48 (2024).
- [150] G. Gerlitz, O. Reiner, and M. Bustin, Microtubule dynamics alter the interphase nucleus, *Cellular and Molecular Life Sciences* **70**, 1255 (2013).
- [151] D. Velasquez-Carvajal, F. Garampon, L. Besnardeau, R. Lemée, S. Schaub, and S. Castagnetti, Microtubule reorganization during mitotic cell division in the dinoflagellate *Ostreopsis cf. ovata*, *Journal of Cell Science* **137**, jcs261733 (2024).
- [152] H. Maiato, P. Sampaio, and C. E. Sunkel, Microtubule-associated proteins and their essential roles during mitosis (Academic Press, 2004) pp. 53–153.
- [153] L. Johannes, W. Pezeshkian, J. H. Ipsen, and J. C. Shillcock, Clustering on membranes: Fluctuations and more, *Trends in Cell Biology* **28**, 405 (2018).
- [154] A. Shrestha, O. Kahraman, and C. A. Haselwandter, Mechanochemical coupling of lipid organization and protein function through membrane thickness deformations, *Physical Review E* **105**, 054410 (2022).
- [155] J. M. Barakat and T. M. Squires, Curvature-mediated forces on elastic inclusions in fluid interfaces, *Langmuir* **38**, 1099 (2022).
- [156] D. Pérez-Sala and M. Guo, Editorial: Intermediate filaments structure, function, and clinical significance, *Frontiers in Cell and Developmental Biology* **10**, 1103110 (2022).
- [157] B. Alberts, A. Johnson, J. Lewis, M. Raff, K. Roberts, and P. Walter, *Molecular Biology of the Cell* (Garland Science, New York, 2002) Chap. The Self-Assembly and Dynamic Structure of Cytoskeletal Filaments, 4th ed.
- [158] F. Brauns, G. Pawlik, J. Halatek, J. Kerssemakers, E. Frey, and C. Dekker, Bulk-surface coupling identifies the mechanistic connection between Min-protein patterns in vivo and in vitro, *Nature Communications* **12**, 3312 (2021).
- [159] L. Würthner, F. Brauns, G. Pawlik, J. Halatek, J. Kerssemakers, C. Dekker, and E. Frey, Bridging scales in a multiscale pattern-forming system, *Proceedings of the National Academy of Sciences* **119**, e2206888119 (2022).
- [160] N. Banterle, A. P. Nievergelt, S. de Buhr, G. N. Hatzopoulos, C. Brillard, S. Andany, T. Hübscher, F. A. Sorgenfrei, U. S. Schwarz, F. Gräter, G. E. Fantner, and P. Gönczy, Kinetic and structural roles for the surface in guiding SAS-6 self-assembly to direct centriole architecture, *Nature Communications* **12**, 6180 (2021).
- [161] W. R. Inc., Mathematica, Version 14.0, champaign, IL, 2024.
- [162] J. Elliott, Elliott2025 mathematica files, <https://git.embl.de/elliott/Elliott2025-Mathematica-Files> (2025).
- [163] M. Olivetta and O. Dudin, The nuclear-to-cytoplasmic ratio drives cellularization in the close animal relative *Sphaeroforma arctica*, *Current Biology* **33**, 1597 (2023).
- [164] A. Ondracka, O. Dudin, and I. Ruiz-Trillo, Decoupling of nuclear division cycles and cell size during the coenocytic growth of the ichthyosporean *Sphaeroforma arctica*, *Current Biology* **28**, 1964 (2018).
- [165] D. Gambarotto, F. U. Zwettler, M. Le Guennec, M. Schmidt-Cernohorska, D. Fortun, S. Borgers, J. Heine, J.-G. Schloetel, M. Reuss, M. Unser, E. S. Boyden, M. Sauer, V. Hamel, and P. Guichard, Imaging cellular ultrastructures using expansion microscopy (u-xm), *Nature Methods* **16**, 71–74 (2018).

Supplementary Material – Repulsive particle interactions enable selective information processing at cellular interfaces

A. Equilibrium distribution of interacting particles

In the following, we derive analytical equations for the equilibrium distributions of diffusive particles on a 2D fluid membrane, which undergo binding/unbinding transitions that are governed by an interaction energy field $\epsilon(\mathbf{r})$. We derive the general equilibrium distribution of particles interacting via a density-dependent interacting potential, first as a solution to the Smoluchowski equations of the system dynamics and then from entropy maximization.

a. Dynamical equations The time evolution of particle densities in the bound, $i = b$, and unbound, $i = u$, states can be described by the reaction-diffusion equation

$$\partial_t \rho_i = \nabla \cdot \left[D_i \nabla (\rho_i) + \beta D_i \rho_i \nabla (E_i + \epsilon_i) \right] + \mathcal{R}_i, \quad (\text{S1})$$

with reaction rates

$$\mathcal{R}_b = f(\rho_u, \rho_b, \epsilon_u) (\kappa_{\text{off}} e^{-\beta(\Delta\epsilon + \Delta E)} \rho_u - \kappa_{\text{off}} \rho_b) \quad (\text{S2})$$

and

$$\mathcal{R}_u = f(\rho_u, \rho_b, \epsilon_u) (\kappa_{\text{off}} \rho_b - \kappa_{\text{off}} e^{-\beta(\Delta\epsilon + \Delta E)} \rho_u), \quad (\text{S3})$$

where $\Delta\epsilon = \epsilon_b - \epsilon_u$, $\epsilon_u \equiv \text{const}$, $\Delta E = E_b - E_u$, and $f(\rho_u, \rho_b, \epsilon_u)$ is a density dependent prefactor that has no effect on the equilibrium densities and is included in $k_{\text{off}} = f(\rho_u, \rho_b, \epsilon_u) \kappa_{\text{off}}$ in the main text. Such equations can be routinely derived from Langevin equations of the particle dynamics as detailed in [63]. For interacting particles, E_i is a particle density-dependent potential field $E_i(\rho_u, \rho_b)$ that takes into account particle-particle interactions. The coarse-graining of interaction potentials into such density-dependent fields is discussed in section B.

We solve these coupled dynamical equations for the equilibrium distribution of particles in the membrane, using no-flux boundary conditions. In equilibrium all fluxes vanish identically, including the reaction rates $\mathcal{R}_i \equiv 0$, which account for fluxes between particle states, and the term $\mathbf{j} = D_i \nabla \rho_i + \beta D_i \rho_i \nabla (E_i + \epsilon_i) = 0$ for the flow of the matter in space. These conditions result in two equilibrium equations:

$$0 = \kappa_{\text{off}} e^{-\beta(\Delta\epsilon + \Delta E)} \rho_u - \kappa_{\text{off}} \rho_b, \quad (\text{S4})$$

and

$$0 = D_i \nabla (\rho_i) + \beta D_i \rho_i \nabla (E_i + \epsilon_i). \quad (\text{S5})$$

The latter condition has the formal solution

$$\rho_i(\mathbf{r}) = \rho_{i,0} e^{-\beta[\epsilon_i(\mathbf{r}) + E_i(\rho_u(\mathbf{r}), \rho_b(\mathbf{r}))]} \quad (\text{S6})$$

where $\rho_{i,0}$ is an integration constant. Substituting this solution into the condition Eq. (S4), we find $\rho_{u,0} = \rho_{b,0}$. With the constants $\rho_{i,0}$ and ϵ_u incorporated into the normalization factor $l^{-2} = \rho_{b,0} e^{-\beta\epsilon_u}$, the equilibrium solutions take the form

$$\rho_u = \frac{1}{l^2} e^{-\beta E_u}, \quad \rho_b = \frac{1}{l^2} e^{-\beta(\Delta\epsilon + \Delta E + E_u)}, \quad (\text{S7})$$

which yield the total particle density

$$\rho = \rho_u + \rho_b = \frac{1}{l^2} e^{-\beta E_u(\rho)} (1 + e^{-\beta(\Delta\epsilon + \Delta E)}). \quad (\text{S8})$$

As shown in the following section, the constant l is related to the chemical potential and can be found from the conservation of the particle number $N = \int dA \rho$ over the whole domain area A .

In the main text, we assume that each particle can exist in either of the two states. In this case $E_u(\rho) = E_b(\rho) = E(\rho)$ and depends only on the total particle density [see sections A b and B a]. Resulting in the equilibrium total particle density

$$\rho = \frac{1}{l^2} e^{-\beta E(\rho)} (1 + e^{-\beta \epsilon}). \quad (\text{S9})$$

where we have set $\Delta\epsilon = \epsilon$ for notation simplicity. Consequences of relaxing this binding site density assumption are discussed in section C 3.

b. Equilibrium solution from entropy maximization Re-deriving the equilibrium solution through entropy maximization provides insight into the origins of the interaction potentials $E_i(\rho_u, \rho_b)$. Here, we obtain equations (S7) by applying the principle of maximum entropy to a system of *indistinguishable* particles with continuous, pairwise-additive interactions and assuming that multiply occupied energy states are allowed. For simplicity, we analyse a one-dimensional system, as the generalization of the simplified model to higher dimensions is straightforward.

In particular, we consider a system divided into B boxes of size dx indexed by $j > 0$ in contact with a reservoir with $j = 0$, characterized by particle number N_0 . Acting as a heat bath, the reservoir can exchange energy, but not particles, with the system. Within each subsystem j there are K_j unbound particles and M_j bound particles. The boxes have degeneracy g_K and g_M of the unbound and bound states with energies ϵ_u (constant) and $\epsilon_{b,j}$ (box-dependent), respectively.

Besides the single-particle contributions of ϵ_b and ϵ_u , we also include an energy term $E_r(K_j, M_j)$, which models local interactions between particles inside each box, as discussed further in Sec. B b. Being local, this term depends only on the number of particles in a given box regardless of their state distributions.

With the above assumptions we can treat the system of particles as a Boltzmann gas. In the microcanonical framework we count the number of microstates W which make up the macrostate defined by $\{K_j, M_j\}$. The number of ways to arrange K_j and M_j indistinguishable particles into g_K and g_M states, respectively, is given by Maxwell-Boltzmann statistics [65, Chapter 13]

$$W_{j \geq 0} = \frac{g_K^{K_j} g_M^{M_j}}{K_j! M_j!}. \quad (\text{S10})$$

Under the imposed constraints of the total energy U and total number of particles N across all boxes, and their number N_0 in the reservoir, the equilibrium state features the maximum number of realizations $W = \prod_{j \geq 0} W_j$ or, equivalently, the maximum Boltzmann entropy $S_B/k_B = \ln W$. We introduce the Lagrange multipliers α , α_0 , β to the constraints on N , N_0 , and U , respectively, and extremize the objective function

$$f(\{K_j\}, \{M_j\}) = \ln W + \alpha \left(N - N_0 - \sum_{j > 0} (K_j + M_j) \right) + \alpha_0 (N_0 - K_0 - M_0) + \beta \left(U - \sum_{j \geq 0} (K_j \epsilon_u + M_j \epsilon_{b,j} + E_r(K_j + M_j)) \right), \quad (\text{S11})$$

by requiring that its derivatives vanish

$$\frac{\partial f}{\partial K_j} = \ln g_K - \ln K_j - \delta_{0j} \alpha_0 - (1 - \delta_{0j}) \alpha - \beta \epsilon_u - \beta \frac{\partial E_r(K_j + M_j)}{\partial K_j} = 0, \quad (\text{S12})$$

$$\frac{\partial f}{\partial M_j} = \ln g_M - \ln M_j - \delta_{0j} \alpha_0 - (1 - \delta_{0j}) \alpha - \beta \epsilon_{b,j} - \beta \frac{\partial E_r(K_j + M_j)}{\partial M_j} = 0, \quad (\text{S13})$$

in which we apply the Stirling approximation, and use the Kronecker δ_{jk} . From Eqs. (S12) and (S13) we obtain

$$K_0 = g_K e^{\beta \left(\mu_0 - \epsilon_u - \frac{\partial E_r(K_0 + M_0)}{\partial K_0} \right)}, \quad M_0 = g_M e^{\beta \left(\mu_0 - \epsilon_{b,0} - \frac{\partial E_r(K_0 + M_0)}{\partial M_0} \right)} \quad (\text{S14})$$

$$K_{j>0} = g_K e^{\beta \left(\mu - \epsilon_u - \frac{\partial E_r(K_j + M_j)}{\partial K_j} \right)}, \quad M_{j>0} = g_M e^{\beta \left(\mu - \epsilon_{b,j} - \frac{\partial E_r(K_j + M_j)}{\partial M_j} \right)} \quad (\text{S15})$$

which represent Boltzmann distribution of particles over energy levels with the chemical potentials of the bath $\mu_0 = -\alpha_0/\beta$ and of the system $\mu = -\alpha/\beta$. The reservoir part of the solution, Eq. (S14)—which we keep for completeness, plays no role in the following.

Now we divide Eq. (S15) by the box size dx , and take the continuum limit $dx \rightarrow 0$ as the number of boxes increases to infinity. This procedure yields the particle densities at $x = \lim_{dx \rightarrow 0} j dx$:

$$\lim_{dx \rightarrow 0} \frac{K_j}{dx} = \rho_u(x) = g_u e^{\beta\mu - \beta\epsilon_u - \beta E(\rho)}, \quad (\text{S16})$$

$$\lim_{dx \rightarrow 0} \frac{M_j}{dx} = \rho_b(x) = g_b e^{\beta\mu - \beta\epsilon_b(x) - \beta E(\rho)}, \quad (\text{S17})$$

with $\rho = \rho_u + \rho_b$ and the implied limits $\lim_{dx \rightarrow 0} \epsilon_{b,j} = \epsilon_b(x)$,

$$\lim_{dx \rightarrow 0} \frac{gK}{dx} = g_u, \quad \lim_{dx \rightarrow 0} \frac{\partial}{\partial(K_j/dx)} \frac{1}{dx} E_r \left[dx \left(\frac{K_i}{dx} + \frac{M_j}{dx} \right) \right] = \frac{\partial}{\partial \rho_u} E_\rho(\rho_u + \rho_b) = \frac{\partial \rho}{\partial \rho_u} \frac{\partial E_\rho(\rho)}{\partial \rho} = E(\rho), \quad (\text{S18})$$

$$\lim_{dx \rightarrow 0} \frac{gM}{dx} = g_b, \quad \lim_{dx \rightarrow 0} \frac{\partial}{\partial(M_j/dx)} \frac{1}{dx} E_r \left[dx \left(\frac{K_j}{dx} + \frac{M_j}{dx} \right) \right] = \frac{\partial}{\partial \rho_b} E_\rho(\rho_u + \rho_b) = \frac{\partial \rho}{\partial \rho_b} \frac{\partial E_\rho(\rho)}{\partial \rho} = E(\rho). \quad (\text{S19})$$

The normalization constant l , introduced in the previous section, can be explicitly related to the chemical potential μ via the formula

$$l = \left(g_u e^{\beta(\mu - \epsilon_u)} \right)^{-\frac{1}{2}},$$

which leads to

$$\rho_u(x) = \frac{1}{l^2} e^{-\beta E(\rho(x))}, \quad \rho_b(x) = \frac{1}{l^2} e^{-\beta(\epsilon_b(x) - \epsilon_u + E(\rho(x)) + k_B T \ln(g_u/g_b))}. \quad (\text{S20})$$

The above equations recapitulate (S7) if we identify $E_u(\rho) = E(\rho)$ and $\Delta E(\rho) = k_B T \ln(g_u/g_b)$. Here we find that, for particles acting as a Boltzmann gas, E_u and E_b remain functions of only the total density ρ , even when relaxing the assumption on binding site density such that the ratio of the densities of states $f_{BS} = g_b/g_u = g_M/g_K < 1$. This ratio characterizes the average number of locally available binding sites, and introduces a constant ΔE , the consequences of which are discussed in section C3.

B. Mean-field potentials for repulsive particle interactions

In this letter we focus on short-range repulsive particle-particle interactions, and first derive the expression for E_u and ΔE in the presence of steric interactions. In this case, the mean-field potential emerges as a correction to the chemical potential of the ideal gas. We then also derive expressions for $E(\rho)$ for other, continuous interactions.

a. Hard-core repulsion In section A, we derived the equilibrium distribution of particles that obey the Maxwell-Boltzmann statistics. Therefore Eq. (S8) corresponds to the distribution of a Boltzmann gas if we set $E(\rho) \equiv 0$. In the presence of steric exclusion effects, we find a correction $\Delta\mu = E(\rho)$ to the chemical potential $\mu^* = \mu + \Delta\mu$. In particular, the lattice gas, where each site of the lattice can host at most one particle of effective size d_0 , models a short-range repulsion mediated by the hard-core potential. This potential is infinite for interparticle separations shorter than d_0 and equals zero otherwise. Such interactions describe particles which effectively exclude the volume they occupy from that available to other particles.

Considering bound and unbound particles in boxes indexed by j as before, we introduce within each box a lattice with a total of Ω sites, of which a subset Q permits the particles to be in the bound state. While the particles are treated as indistinguishable, the sites are not. We count the number of microstates W that make up the macrostate defined by K_j, M_j by first counting the arrangements of the bound particles. These can occupy any of the Q sites, but no site can have more than one particle, resulting in the number of combinations of the M_j indistinguishable particles

$$W_{M,j} = \frac{Q!}{(Q - M_j)! M_j!}. \quad (\text{S21})$$

Next, we count the possible arrangements for the free particles. For a total of Ω sites within the lattice, M_j of which are already occupied, there remain $\Omega - M_j$ available spaces. Therefore the number of arrangements for the free particles is given by

$$W_{K,j} = \frac{(\Omega - M_j)!}{(\Omega - M_j - K_j)!K_j!}. \quad (\text{S22})$$

The number of microstates for one box is then the product of equations (S21) and (S22),

$$W_j = W_{K,j}W_{M,j} = \frac{Q!(\Omega - M_j)!}{(Q - M_j)!(\Omega - M_j - K_j)!K_j!M_j!}. \quad (\text{S23})$$

Extremizing $\ln W = \sum_{j \geq 0} \ln W_j$ subject to the same constraints of energy and particle numbers as before yields

$$K_j = (\Omega - M_j - K_j)e^{-\delta_{0j}\alpha_0 - (1 - \delta_{0j})\alpha - \beta\epsilon_u}, \quad (\text{S24})$$

$$M_j = (\Omega - M_j - K_j)\frac{Q - M_j}{\Omega - M_j}e^{-\delta_{0j}\alpha_0 - (1 - \delta_{0j})\alpha - \beta\epsilon_{b,j}}. \quad (\text{S25})$$

Although Eqs. (S24) and (S25) can be explicitly solved for K_j and M_j , leading to a Fermi-Dirac-like distribution, we keep the K_j - and M_j -dependent prefactors in the form convenient to determine the Lagrange multiplier $\alpha = -\beta\mu^*$ related to the chemical potential μ^* of the hard-core lattice gas. In the continuum limit $dx \rightarrow 0$, cf. Eqs. (S16) and (S17), we obtain thus

$$\rho_u(x) = (\rho_{\max} - \rho_b(x) - \rho_u(x))e^{-\alpha - \beta\epsilon_u} \quad (\text{S26})$$

$$\rho_b(x) = (\rho_{\max} - \rho_b(x) - \rho_u(x))\frac{\rho_{\text{ext}} - \rho_b(x)}{\rho_{\max} - \rho_b(x)}e^{-\alpha - \beta\epsilon_b(x)} \quad (\text{S27})$$

where $\rho_u(x)$ and $\rho_b(x)$ are the densities of unbound and bound particles, and $\rho_{\max} = 1/d_0^2 = \lim_{dx \rightarrow 0} \Omega/dx$ and $\rho_{\text{ext}} = \lim_{dx \rightarrow 0} Q/dx$ are the maximum-packing and binding-site densities respectively. C.f. Eq. (S7), we find

$$E_u(\rho) = -k_B T \ln \left(1 - \frac{\rho}{\rho_{\max}} \right) \quad (\text{S28})$$

and

$$\Delta E(\rho) = -k_B T \ln \left(\frac{\rho_{\text{ext}} - \rho_b}{\rho_{\max} - \rho_b} \right), \quad (\text{S29})$$

for $l^2 = e^{\alpha + \beta\epsilon_u}/\rho_{\max}$, where the discrepancy between the number of lattice sites and the number of binding sites introduces a dependence of ΔE on the density of bound particles. The assumption that each particle has exactly one binding site is equivalent to the assumption that the binding site density is equal to the maximum particle density (i.e. $\rho_{\max} = \rho_{\text{ext}}$). Under this assumption, $\Delta E = 0$ and $E_u(\rho) = E(\rho)$, and we recover Eq. S9 from Eqs. (S26) and (S27). The consequences of foregoing this simplifying assumption are addressed in Sec. C3.

b. Soft-core repulsion Next we demonstrate how generic soft-core repulsive interactions give rise to a density-dependent mean-field potential $E(\rho)$. In Sec. A b, we obtained $E(\rho) = \partial_\rho E_\rho(\rho)$ from the local many-body interaction $E_r(K_j + M_j)$ in the continuum limit of the coarse-graining box size $dx \rightarrow 0$. Considering now two-dimensional boxes of size $a = dx^2$, we assume a pairwise-additive form of the interparticle potential, neglect non-nearest neighbor interactions, and approximate the pairwise distances between neighboring particles m and k by their average, i.e. $d_{mk} \approx d = \sqrt{a/N_j}$, given a uniform distribution of particles in the box. With ξ denoting the number of nearest neighbors, the interparticle potential in the j th box and its derivative are given by

$$E_r(N_j) \approx N_j \frac{\xi}{2} u(d), \quad (\text{S30})$$

$$\frac{\partial E_r(N_j)}{\partial N_j} \approx \frac{\xi}{2} \left(u(d) + N_j \frac{\partial u(d)}{\partial d} \frac{\partial d}{\partial N_j} \right) = \frac{\xi}{2} u(d) - \frac{\xi}{4} \frac{\partial u(d)}{\partial d} d, \quad (\text{S31})$$

which in the continuum limit reads

$$E(\rho) = \frac{\partial E_\rho(\rho)}{\partial \rho} = \frac{\xi}{2} u(d) - \frac{\xi}{4} \frac{\partial u(d)}{\partial d} d, \quad (\text{S32})$$

with $d = \sqrt{1/\rho}$.

Similar interaction potentials arise from other physical repulsion mechanisms, for example due to membrane-curvature mediated interactions, or shielded electrostatic interactions. Curvature mediated repulsive interactions can be approximated as pairwise additive at low particle densities, given by [50]

$$u_{\text{curvature}}(d_{mk}) = 8\pi\kappa\theta^2 \left(\frac{d_0}{2d_{mk}} \right)^4, \quad (\text{S33})$$

where θ is the membrane contact angle, and κ denotes the membrane bending rigidity [51], leading to the mean-field potential

$$E_{\text{curvature}}(d) = 24\pi\kappa\theta^2 \frac{\xi}{2} \left(\frac{d_0}{2d} \right)^4. \quad (\text{S34})$$

Similarly, shielded electrostatic interactions described by the Yukawa potential [52, 53] lead to an interaction energy

$$u_{\text{electrostatic}}(d_{mk}) = \frac{Q^2}{4\pi\epsilon_0} \frac{e^{-d_{mk}/\lambda_d}}{d_{mk}}, \quad (\text{S35})$$

where the vacuum permittivity is $\epsilon_0 = 55.2 \text{e}^2 \text{eV}^{-1} \mu\text{m}^{-1}$, which can be written in units of $K_{\text{B}}T$, for $T = 300 \text{K}$, as $\epsilon_0 = 2.14 \times 10^6 \text{e}^2 k_{\text{B}}T^{-1} \text{nm}^{-1}$. The corresponding mean-field potential reads

$$E_{\text{electrostatic}}(d) = \frac{\xi}{2} \frac{Q^2}{4\pi\epsilon_0} \frac{e^{-d/\lambda_d}}{d} \left(\frac{3}{2} + \frac{d}{2\lambda_d} \right). \quad (\text{S36})$$

In Fig. 1(b), we show the comparison between Eqs. (S36), (S34), and (S28) using a particle size $d_0 = 1 \text{nm}$, which is the typical order of magnitude for protein size [54, pg. 45] [55, BNID 100018], and assuming the number of nearest neighbors to be $\xi = 6$. For the curvature-mediated interactions we use the membrane bending rigidity $\kappa = 20 k_{\text{B}}T$ [56] and the membrane contact angle $\theta \approx \pi/24$, and for the electrostatic interactions we use the Debye length $\lambda_d = 0.8 \text{nm}$ [57] and consider particles with a charge of four elementary charges, $Q \approx 4e$.

C. Quantification of information transmission

As discussed in the main text, the binding energy fields contain information on the physical properties of the environment, which is selectively encoded by the particle density distribution. We ask how *fluctuating* particle densities respond to variations in the binding energy field across different environments, and characterize how much information the densities carry about the external binding energy, given the compression that results from the sigmoidal relation Eq. (6). To ease analysis and allow verification by Metropolis sampling, we compute the relevant probability distributions and the mutual information between the input energy and the output particle density by discretizing these quantities, and introducing random vectors with realizations $\{\rho_j\}$ and $\{\epsilon_k\}$ with box indices $j, k = 1, \dots, B$. The calculations detailed in this section were implemented in Mathematica [161], the notebooks of which are provided in the repository [162].

1. Gaussian approximation of particle fluctuations

Similar to before, we discretize our surface into boxes of area a indexed by j , and now introduce a random vector for the particle numbers, with one entry per box, denoting a given realization by $\{N_j\}$. In the grand canonical ensemble,

fluctuations in the total number of particles $\{N_j\}$ in all the boxes obey the distribution $P(\{N_j\}) \propto e^{S/k_B}$, where S is the entropy of the system and the reservoir. We find the entropy $S = k_B \ln W$ from the number of microstates W . To obtain an approximate expression for the particle number fluctuations, we do not distinguish between bound and unbound particles, in contrast to section A, such that the number of particle arrangements is given by

$$W = \prod_j \frac{\Omega!}{(\Omega - N_j)! N_j!}, \quad (\text{S37})$$

resulting in the probability of a given set of particle numbers following

$$P(\{N_j\}) \propto \prod_j e^{\Omega(\ln \Omega - 1) - (\Omega - N_j)(\ln(\Omega - N_j) - 1) - N_j(\ln N_j - 1)}, \quad (\text{S38})$$

in which we have applied the Stirling approximation. By applying the saddle-point approximation about the most likely values \bar{N}_j [73], we get

$$\ln P(\{N_j\}) \asymp \sum_j \frac{1}{2} \left(\frac{\partial^2 \ln P}{\partial N_j^2} \Big|_{N_j = \bar{N}_j} (N_j - \bar{N}_j)^2 \right), \quad (\text{S39})$$

in which the first-order derivatives vanish, as well as the cross-term $\partial \ln P(\{N_j\}) / (\partial N_j \partial N_{k \neq j})$. Note that this approximation treats the particle number fluctuations in each box as independent, since Eq. (S39) implies $P(\{N_j\}) = \prod_j P(N_j)$. By substituting (S38) into (S39) and identifying the discrete densities $\rho_j = N_j/a$ and $\bar{\rho}_j = \bar{N}_j/a$, and $\Omega = a/d_0^2$, we evaluate the derivative as

$$\sum_j \frac{\partial^2 \ln P}{\partial N_j^2} \Big|_{N_j = \bar{N}_j} \frac{(N_j - \bar{N}_j)^2}{2} = - \sum_j \frac{\Omega}{(\Omega - N_j) N_j} \Big|_{N_j = \bar{N}_j} \frac{(N_j - \bar{N}_j)^2}{2} = - \sum_j \frac{a}{(1 - d_0^2 \bar{\rho}_j) \bar{\rho}_j} \frac{(\rho_j - \bar{\rho}_j)^2}{2}. \quad (\text{S40})$$

From Eqs. S39-S40, and taking into account the dependence of the mean $\bar{\rho}_j$ on the binding energy, we obtain the following expression for the conditional probability of a given particle density in box j

$$P(\rho_j | \{\epsilon_k\}) \propto \exp \left[- \frac{(\rho_j - \bar{\rho}_j(\{\epsilon_k\}))^2}{2\sigma_\rho^2(\{\epsilon_k\})} \right] \quad (\text{S41})$$

with variance $\sigma_\rho^2(\{\epsilon_k\}) = [1 - d_0^2 \bar{\rho}_j(\{\epsilon_k\})] \bar{\rho}_j(\{\epsilon_k\})/a$ and mean $\bar{\rho}_j(\{\epsilon_k\})$ [Eq. (6)], where $\{\epsilon_k\}$ denotes the vector of input energy values. The mean depends on the full set of realizations in all boxes $\{\epsilon_k\}$ through the constraint of particle conservation, Eq. (3), which in the discrete limit takes the form

$$\sum_j \bar{\rho}_j(\{\epsilon_k\}) = \frac{B}{\bar{d}^2}. \quad (\text{S42})$$

Note that our approximation of the variance σ_ρ^2 neglects any explicit dependence of the particle fluctuations on the binding energy.

a. Metropolis sampling To investigate the validity of our approximation for $P(\rho_j | \{\epsilon_k\})$, we numerically estimate the conditional probability Eq. S41 by performing Metropolis-Hastings sampling of the distribution of particles given a fixed set of input energies (code provided in [74]). On a 100-by-100 lattice, where the box index j can be identified with a lattice coordinate (v, w) , we fix the input energy to a linear profile $\epsilon_{vw} = (2v/10 - 10)k_B T$, and sample the particle distributions for 1000, 5000, and 9000 particles, which in terms of $(d_0/\bar{d})^2$ correspond to the values 0.1, 0.5, and 0.9 respectively. We discretize the possible binding energies into 241 evenly-spaced values between $-12k_B T$ and $12k_B T$, and add a Gaussian noise with standard deviation $1 k_B T$. The sampled particle densities, resolved along the v -axis, are shown together with the analytical density profiles in Fig. 2(a). We compare the sampled local conditional probability for the $(d_0/\bar{d})^2 = 0.5$ case with Eq. (S41) (Fig. S1), and find that, as expected, the high-density region has a lower channel noise than the low-density region where the number of possible particle configurations over the available distinguishable energy levels is larger. We observe a good agreement between the simulations and the Gaussian approximation Eq. (S41), especially for low and high densities.

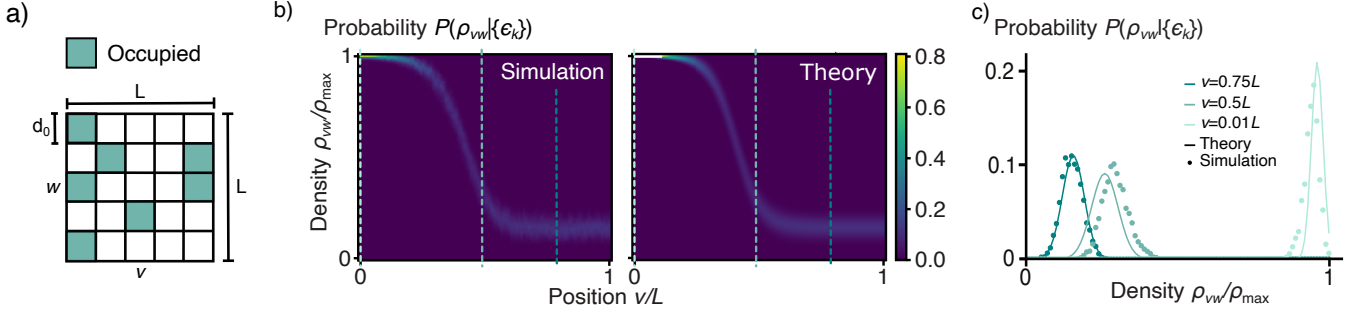


FIG. S1. The conditional probability $P(\rho_j|\{\epsilon_k\})$ is well approximated by a Gaussian distribution Eq. S41. a) Sketch of lattice setup for Metropolis-Hastings simulations. b) Comparisons of the estimates for $P(\rho_{vw}|\{\epsilon_{vw}\})$ from simulations (left) and the Gaussian approximation (right) for $(d_0/\bar{d})^2 = 0.5$ and input energy $\epsilon_{vw} = (2v/10 - 10)k_B T$. Colored dashed lines mark positions plotted in (c), and white shading indicates values above 0.8. c) The conditional distribution estimates at various positions show that the Gaussian expression approximates the simulated system well for mean densities at the two plateaus, while a slight shift appears in at intermediate positions.

b. Joint probability of particle density and binding energy The joint probability $P(\{\rho_j\}, \{\epsilon_k\}) = P(\{\rho_j\}|\{\epsilon_k\})P(\{\epsilon_k\})$ of observing a particular set of density values $\{\rho_j\}$ together with an input energy vector $\{\epsilon_k\}$, is the product of the conditional probability $P(\{\rho_j\}|\{\epsilon_k\})$ and the marginal probability of the input $P(\{\epsilon_k\})$. To investigate how well the particle patterns distinguish between different inputs, we define the support of the distribution $P(\{\epsilon_k\})$ to include all possible inputs that the surface could receive, i.e. to keep the framework general, we assume the elements of the vector $\{\epsilon_k\}$ to be independently and uniformly distributed as $P(\epsilon_k) = 1/n$, where n is the number of possible energy levels so that

$$P(\{\epsilon_k\}) = \prod_k^B P(\epsilon_k) = n^{-B}. \quad (\text{S43})$$

Similarly, the conditional probability $P(\{\rho_j\}|\{\epsilon_k\})$ of a density profile $\{\rho_j\}$ given an input energy profile $\{\epsilon_k\}$ can be calculated as the product of the local conditional probability $P(\rho_j|\{\epsilon_k\})$ – given by Eq. (S41) – over the whole space

$$P(\{\rho_j\}|\{\epsilon_k\}) = \prod_j^B P(\rho_j|\{\epsilon_k\}), \quad (\text{S44})$$

such that the joint probability distribution takes the form

$$P(\{\rho_j\}, \{\epsilon_k\}) = \frac{1}{n^B} \prod_j^B P(\rho_j|\{\epsilon_k\}). \quad (\text{S45})$$

For completeness we remark that in the continuum limit $a \rightarrow 0$ and $B \rightarrow \infty$ Eq. (S45) yields a functional

$$P[\rho(\cdot), \epsilon(\cdot)] \propto g_{\text{DOS}} \exp \left\{ \int_A dA \ln P[\rho(\mathbf{r})|\epsilon(\cdot)] \right\}.$$

where g_{DOS} is the constant density of energy states, and the integral is taken over the area A of the domain.

2. Mutual information between energy and particle densities

The information gained about the input field by observing the output density field is given by the mutual information [107, Chapter 2]

$$I = \sum_{\{\epsilon_k\}} \sum_{\{\rho_j\}} P(\{\rho_j\}, \{\epsilon_k\}) \ln \frac{P(\{\rho_j\}, \{\epsilon_k\})}{P(\{\rho_j\})P(\{\epsilon_k\})}. \quad (\text{S46})$$

Here $\sum_{\{\epsilon_k\}} = \sum_{\epsilon_1} \sum_{\epsilon_2} \dots \sum_{\epsilon_B}$ and $\sum_{\{\rho_j\}} = \sum_{\rho_1} \sum_{\rho_2} \dots \sum_{\rho_B}$ denote sums over all possible realizations of the input and output random vectors respectively, and the marginal probability $P(\{\rho_j\}) = \sum_{\{\epsilon_k\}} P(\{\rho_j\}, \{\epsilon_k\})$, can be found by summing the joint probability over all combinations of possible input vectors. With Eq. (S45), (S46) then reads

$$I = \frac{1}{n^B} \sum_{\{\epsilon_k\}} \prod_j \sum_{\rho_j} P(\rho_j | \{\epsilon_k\}) \ln \prod_m \frac{P(\rho_m | \{\epsilon_k\})}{\sum_{\{\epsilon_\eta\}} P(\rho_m | \{\epsilon_\eta\}) \prod_\nu P(\epsilon_\nu)}, \quad (\text{S47})$$

in which we used that $\sum_{\{\rho_j\}} = \prod_j \sum_{\rho_j}$. The product over m in the above equation runs over terms that depend on a single possible value of the density ρ_m , which allows us to write

$$\begin{aligned} & \prod_j \sum_{\rho_j} P(\rho_j | \{\epsilon_k\}) \ln \prod_m \frac{P(\rho_m | \{\epsilon_k\})}{\sum_{\{\epsilon_\eta\}} P(\rho_m | \{\epsilon_\eta\}) \prod_\nu P(\epsilon_\nu)} \\ &= \sum_m \left[\prod_{j \neq m} \sum_{\rho_j} P(\rho_j | \{\epsilon_k\}) \right] \sum_{\rho_m} P(\rho_m | \{\epsilon_k\}) \ln \frac{P(\rho_m | \{\epsilon_k\})}{\sum_{\{\epsilon_\eta\}} P(\rho_m | \{\epsilon_\eta\}) \prod_\nu P(\epsilon_\nu)} \\ &= \sum_m \sum_{\rho_m} P(\rho_m | \{\epsilon_k\}) \ln \frac{P(\rho_m | \{\epsilon_k\})}{\sum_{\{\epsilon_\eta\}} P(\rho_m | \{\epsilon_\eta\}) \prod_\nu P(\epsilon_\nu)}, \end{aligned} \quad (\text{S48})$$

where the factor in the brackets evaluates to one due to the normalization of probabilities $\sum_{\rho_j} P(\rho_j | \{\epsilon_k\}) = 1$. By substituting Eq. (S48) into (S47) and expanding the joint probability $P(\rho_m, \{\epsilon_\eta\}) = P(\rho_m | \{\epsilon_\eta\}) \prod_\nu P(\epsilon_\nu) = P(\rho_m | \{\epsilon_\eta\})(1/n^B)$, the mutual information takes the form

$$I = \frac{1}{n^B} \sum_{\{\epsilon_k\}} \sum_m \left[\sum_{\rho_m} P(\rho_m | \{\epsilon_k\}) \ln \frac{P(\rho_m | \{\epsilon_k\})}{\sum_{\{\epsilon_\eta\}} P(\rho_m | \{\epsilon_\eta\})(1/n^B)} \right]. \quad (\text{S49})$$

Finally, since all elements of $\{\epsilon_k\}$ are identically distributed, the expression inside the brackets depends on the box index m only through ρ_m , implying that this term takes the same value regardless of the value of m . Therefore the mutual information reads

$$I = \frac{B}{n^B} \sum_{\{\epsilon_k\}} \left(\sum_{\rho_m} P(\rho_m | \{\epsilon_k\}) \ln \frac{P(\rho_m | \{\epsilon_k\})}{\sum_{\{\epsilon_\eta\}} P(\rho_m | \{\epsilon_\eta\})(1/n^B)} \right). \quad (\text{S50})$$

This last equation was evaluated for a system with coarse-graining area $a = 10d_0^2$ and $B = 5$. We constructed all possible input vectors given a minimum interaction energy of $-10k_B T$ (a typical chemical-interaction potential between biological proteins), an upper cutoff $+10k_B T$, and discretizing the possible levels to integer values in units of $2k_B T$, such that each element ϵ_j was sampled from the set $\mathcal{E} = \{-10k_B T, -8k_B T, \dots, 10k_B T\}$. We discretized the possible density values according to the number of particles in the coarse-graining area a , such that the value of each density element is sampled from the set $\{0, d_0^2/a, 2d_0^2/a, \dots, 1\}$. Calculating the corresponding value of $P(\rho_m | \{\epsilon_k\})$ —as given by Eq. (S41)—for each possible value of ρ_m then permitted the evaluation of Eq. (S50).

3. Influence of binding site density and heterogeneity on information transmission

Equation (S9) from section A is valid under the assumption that the interaction sites, or binding sites, are uniformly distributed with the same density as the maximum density of the particles, such that each particle can exist in either a bound or unbound state. Relaxing this assumption, and introducing a uniform area fraction of binding sites $f_{BS} = \rho_{ext}/\rho_{max}$, Eqs. (S26) and (S27) yield the total equilibrium particle density

$$\rho(x) = \frac{\rho_{max}}{1 + e^{\alpha + \beta \epsilon_u}} \left(1 + f_{BS} \frac{e^{\alpha + \beta \epsilon_u}}{e^{\beta \epsilon(x)} + 1 + e^{\alpha + \beta \epsilon_u + \beta \epsilon(x)}} \right), \quad (\text{S51})$$

and we find that a reduction in the uniform binding site density results in a smaller separation between the maximum and minimum densities, and a smaller gain, leading to reduced information transmission (Fig. S2). However, cellular

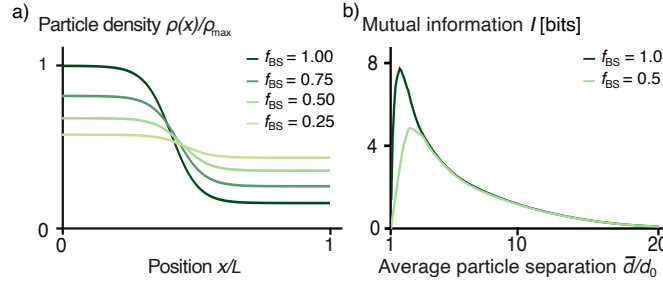


FIG. S2. Reducing the *uniform* binding site density reduces the amount of information read out via the particle density. a) Equilibrium particle density profiles forming in response to a linear input energy profile $\epsilon(x) = (20x/L - 10)k_bT$ over a domain of length L show that reducing the area fraction f_{BS} lowers the gain of the filter. b) The reduced gain leads to a lower mutual information for uniform binding sites with $f_{BS} = 0.5$ compared to $f_{BS} = 1$.

structures at membranes have typically irregular shapes – membrane-bound proteins, for example, often interact with slender cytoskeletal filaments. Considering a non-uniform area-fraction $\phi = \zeta L d_0 / A = \zeta d_0 / L$ for binding sites arranged along ζ parallel lines of length L and with the width of a single particle d_0 , we divide the membrane into parallel strips of width d_0 , and consider the set of line-densities ρ_{1D} obtained by taking the integral of the 2D particle density over the width of each strip. The constant l defined by particle conservation across the whole surface is then determined through

$$\frac{\phi}{L d_0} \left(\int_0^L dx \rho_{1D}(x) \right) + \frac{1 - \phi}{l^2 + d_0^2} = \frac{1}{\bar{d}^2}, \quad (\text{S52})$$

in which x parameterizes the coordinates along the ζ lines, within which $\epsilon = \epsilon(x)$, and the interaction energy is infinite within the remaining region. We compare the information transmission capacity of such nonuniform area fraction systems to the uniform case by evaluating (S50) along strips discretized into $B = 5$ segments of length $10d_0$, such that the coarse-graining area remains $a = 10d_0^2$, and use the same discretization of energy and density values as before. We find that for filament-like input binding structures a smaller number of particles are required for effective information transfer compared to uniform surfaces, since the membrane regions without binding sites act as a particle bath for the regions with binding sites. Although we consider parallel lines for analytical convenience, our findings hold for non-overlapping lines of any orientation.

D. Estimating the effective size and average spacing of particle-like structures at cellular membranes

The properties of the sigmoidal mapping that arises between binding energy and particle distribution due to repulsive interactions are determined by the gain and threshold parameters, which are in turn set by the effective particle size d_0 and their average spacing \bar{d} . Table S1 shows measured or estimated values for these parameters for a range of protein complexes and macromolecular complexes, together with the corresponding sources. We aimed to compile an exhaustive list of proteins and subcellular structures for which this information is currently available – no selection was made beyond restricting the search to *membrane-bound* particle-like structures. Fig. 2(c) shows these compiled parameter values together with the optimal information-processing regime for an actin-like area fraction of binding sites $\phi = 10^{-2}$. This estimate is based on measurements of cortical actin filament densities obtained from high-resolution cryo-ET tomograms in fibroblasts ([75, Fig. 2(c)]).

E. Distribution of nuclear pore complexes in the nuclear envelope of the ichthyosporean *S. arctica*

To test our predictions for the mapping between interaction energy fields and particle density profiles, we measured the distribution of nuclear pore complexes (NPCs) in the nuclei of the multinucleate unicellular organism *Sphaeroforma arctica* [59, 163]. NPCs are embedded within the double-bilayer membrane of the nuclear envelope (NE), and associate

Protein structure	Average density $1/\bar{d}^2$ [μm^{-2}]	Average separation \bar{d} [nm]	Interaction length d_0 [nm]
Integrin LFA-1	120 [76]	91	10 [77]
Integrin VLA-4	75 [76]	115	10 [77]
E-Cadherin	630 [78]	40	7 [78]
TCR	42.4 [79, 80, BNID 103567]**	154	10 [81]*
ICAM-1	900 [82]	33	3 [83]*
Connexons	5000 [84]	14	9.5 [85]
Piezo-1	0.52 [86]	1387	24 [87]
Caveolae	0.04 [88]	5000	75 [89]
VDAC	5000 [90]	14	3.8 [91]
ERMES	1200 [92]	29	15 [92]
Lipid GM1	17000 [93]**	8	3 [94]
AChR	55 [95, 96]**	135	10 [97, 98]
Fc γ -1	11 [99, 100]**	302	2.7 [101, BNID 117058]*
EGFR	636 [102]	40	17 [103]
Focal adhesions	0.14 [104, 105]**	2673	700 [104]
NPCs	-	440 ***	260 ***

TABLE S1. Reported parameters for particle-like structures at cellular and subcellular membrane surfaces.

* $d_0 = 2r_{\min}$ with r_{\min} calculated from molecular mass value using [106]. ** Calculated as number of protein complexes per area of a spherical cell of a given diameter. *** Measured in our study.

with microtubules (MTs) that emanate from microtubule organising centers (MTOCs) at the nuclear poles in a regular, radial fashion in this system (Fig. 3(a),[60]).

1. Experimental methods

a. Culture conditions *Sphaeroforma arctica* was cultured at 17 °C in Marine broth (Difco, 37.4 g l⁻¹) and synchronized as previously described [59, 164]. Briefly, the cultures were synchronized in 1/16 Marine broth diluted in artificial seawater (Instant Ocean, 37 g l⁻¹). Cultures were diluted 1:100 in 1/16 Marine broth and grown for 3 days to obtain synchronised cultures. The synchronised cultures were inoculated 1:50 in fresh 10ml Marine broth in 25ml cell culture flasks. To obtain the 8-32 nuclear stage, cells were fixed around 28 - 30h after inoculation. The cell culture flasks were scraped and the suspension was added to 15 ml Falcon tubes and collected by centrifugation at 500rpm for 5 min. The supernatant was removed and cells were transferred to 1.5 ml microfuge tubes and fixative was added for 30 min. The cells were fixed with 4% formaldehyde in 250 mM sorbitol in 1× phosphate buffer saline (PBS), washed twice with PBS and resuspended in 20-30 μl of PBS.

b. Ultrastructure expansion microscopy Ultrastructure expansion microscopy (U-ExM) was performed as previously described [60, 165]. Briefly, the fixed cells were anchored in 1% acrylamide/ 0.7% formaldehyde solution overnight at 37 °C. The anchored cells were attached to 6 mm poly-l-lysine-coated coverslips for 30 mins - 1 h. The coverslips with cells were inverted on a 9 μL drop of monomer solution (19% (wt/wt) sodium acrylate (7446-81-3), 10% (wt/wt) acrylamide (Sigma-Aldrich A4058), 0.1% (wt/wt) N,N'-methylenebisacrylamide (Sigma-Aldrich M1533) in PBS). After a 5 min incubation on ice, gels were allowed to polymerize for 1 h at 37 °C in a moist chamber. For denaturation, coverslips along with gels were transferred to the microfuge tubes with 1 ml pre-heated denaturation buffer (50 mM Tris pH 9.0, 200 mM NaCl, 200 mM SDS, pH to 9.0) and incubated at 95 °C for 1.5 hours. Following denaturation, the gels were expanded with 3 water exchanges as previously described. Post expansion, the gel diameter was measured and used to determine the expansion factor.

c. Immunostaining and imaging For staining, the gels were re-incubated in 1x PBS to shrink them. This was followed by blocking in 3% bovine serum albumin (BSA) in PBST (1× PBS with 0.1% Tween20) at room temperature for 30min - 1h. The gels were then incubated for 5 h at 37 °C in primary antibody [Tubulin - AA344 and AA345 (ABCD antibodies) and NPC - MAb414 (Biolegend 902901)] prepared at 1:500 in blocking solution. This was followed by three washes for 10 min at room temperature in PBST and addition of the secondary antibody [Goat anti-mouse secondary antibody, Alexa Fluor 488 (Thermo A-11001), Goat anti-guinea pig secondary antibody, Alexa Fluor 647 (Thermo A-21450)] at 1:500 final concentration in blocking solution. Incubation was done at 4 °C overnight. Next

gels were stained with protein and lipid pan-labelling dyes, Dylight 405 (ThermoFischer, 46400) and BODIPY TR ceramide (ThermoFischer D7540, 2 mM stock in dimethylsulfoxide), at 1:500 dilution in $1 \times$ PBS for 2 – 5 h. The gels were then washed and re-expanded prior to imaging. Ibidi chamber slides (two-well, Ibidi 80286) were pre-coated with poly-l-lysine. Gels were cut to an appropriate size to fit the Ibidi chambers and added onto the wells. The gels were overlaid with water to prevent drying or shrinkage during imaging. The gels were imaged using the Zeiss LSM 880 with the Airy fast mode using a Plan-Apochromat $63 \times / 1.4$ Oil DIC M27. The images were processed with the default 3D airsacan processing on the ZEN software prior to further analysis.

2. Image analysis and parameter estimation

We estimated i) the distance between the MTs and the NE, and ii) the NPC coordinates in the NE as detailed in our protocol [140]. Briefly, we traced MT filaments from their point of origin at the MTOC (identified manually) using Sato and Frangi tubeness filters, skimage.morphology’s skeletonize.3d function, and a custom algorithm for connecting branches into their most likely filament combinations, which attaches branch ends that are close to each other and aligned in the same direction, allowing for the correction of patchy MT labelling [Fig. S3(a)]. Segmenting the nuclei using a Hessian filter on the membrane channel, we then calculated the shortest distance from the NE to coordinates along each filament, neglecting all filaments from nuclei with major segmentation or tracing errors and applying selection criteria on the total length of the filaments ($> 1.1 \mu\text{m}$) and their proximity to the NE ($< 0.3 \mu\text{m}$ over the nearest $1.1 \mu\text{m}$ to the MTOC). This analysis allowed the estimation of the average area-fraction of NE-proximal MT filaments on the nuclear envelope, $\phi = (0.21 \pm 0.03)$ (used in Fig. 3(e)). Applying a further selection criteria on the total length of the profiles ($> 3.4 \mu\text{m}$, resulting in 110 individual height profiles), we clustered the profiles into nine groups using agglomerative clustering, considering a region of interest (ROI) defined as the segment between $0.2 \mu\text{m}$ and $3.8 \mu\text{m}$ from the MTOC. To this end, we computed the dissimilarity matrix for the dataset, in which the dissimilarity score for a pair of profiles is given by

$$\text{Dissimilarity Score} = \frac{\sum_k^{\text{Min}(N_{pi}, N_{pj})} |(h_{i,k} - h_{j,k})|}{\text{Min}(N_{pi}, N_{pj})} \quad (\text{S53})$$

where k indexes the pixels and N_{pi} denotes the total length of the i th profile h_i . For the subsequent parameter fitting, we excluded clusters containing fewer than five filaments or which had a dissimilarity score larger than 4000.

We identified the coordinates of approximately all NPCs on the NE surface by thresholding the NPC channel [Fig. S3(a)], from which we estimated their average spacing over all the nuclei as $\bar{d} = (440 \pm 50) \text{ nm}$, and over the nuclei that contribute filaments to each cluster (weighted by the number of filaments contributed) as given in S3. To compute the 1D line-densities along the MT filaments, we counted NPCs within a 160 nm interval around each filament’s shortest-distance projection line.

a. Parameter fitting We approximated the interaction energy between an NPC and its binding site on a nearby MT by a chemical interaction energy $\epsilon_c = 25k_B T$ ([141]) and an elastic Hookean contribution, where we represented the combined elastic contributions arising from local deformations of the nuclear envelope, stretching of the linker complex, and deflection of the microtubule with the effective elastic interaction term $\lambda(\hat{h}(s) - h_0)^2/2$, in which we included the resting length of the effective spring $h_0 \approx (84 \pm 15) \text{ nm}$, estimated by measuring the minimum NPC-MT separation distance within the high-density regions of our ROIs from electron microscopy images (Table S2,[60]). We estimated the effective spring constant λ and the effective particle size d_0 for the MT-NPC system by minimizing the objective function

$$J(\rho, \hat{\rho}; \lambda, d_0) = \sum_i (\hat{\rho}_i - \rho(\hat{s}_i; \lambda, d_0))^2, \quad (\text{S54})$$

in which $\hat{\rho}$ denotes the measured density at the arc-length position \hat{s} , and ρ was computed by evaluating Eq. (6) at \hat{s}_i . We fitted our parameters independently for each cluster, performing a rational-exponential reparameterization of the measured height profiles to obtain a differentiable representation of the data \hat{h} [Fig. S3(b), Fig. 3(c)], and calculating the average NPC separation \bar{d} and average number of filaments per nuclear area ζ/A independently for each cluster. The resultant estimates from each cluster are summarized, along with the corresponding \bar{d} and ζ/A values, in Table S3. While the effective particle sizes were well-constrained across the different MT profiles, the cost functions featured shallow regions extended in the direction of the spring constant parameter in some cases, showing

Effective spring rest length h_0 [nm]	Effective particle size d_0 [nm]
71	266
90	236
89	222
110	183
75	156
80	161
87	163
81	141
71	224
85	249
85	235
88	186
65	228
70	178
94	187
83	135
85	151
88	169
91	177
83	229
110	200
91	162
108	190
57	170
66	184

TABLE S2. Parameter estimates from electron tomograms of *Sph. arctica* nuclei [60].

Cluster	Average particle separation d [nm]	Average number of filaments per nuclear area ζ/A [μm^{-2}]	Fitted effective particle size d_0 [nm]	95% CI d_0 [nm]	Fitted effective spring constant λ [pN nm $^{-1}$]	95% CI λ [pN nm $^{-1}$]
1	443	0.27	310	{350, 260}	0.036,	{0.029, >0.109}
2	451	0.27	310	{340, 280}	0.024	{0.020, >0.109}
3	437	0.30	230	{260, 200}	0.090	{0.084, >0.109}
4	452	0.30	200	{240, 180}	0.030	{0.028, 0.032}
5	466	0.28	240	{250, 220}	0.026	{0.025, 0.059}

TABLE S3. Parameter estimates obtained by measurement or by minimizing the cost function Eq. S54 for five different proximity profiles of microtubules.

that the fit quality has limited sensitivity to variations in this parameter within the explored range. Nonetheless, we obtained consistent estimates for the spring constants from the five distinct MT datasets. Note that using the effective elastic interaction to account for the binding interactions between NPCs and MTs neglects any changes in h due to binding of the nuclear pore complexes beyond what is accounted for through the effective spring constant λ , i.e. we assume that the MT network maintains an overall fixed morphology.

To assess the validity of our fit, we used electron tomograms from [60] to independently measure the effective NPC particle size d_0 . Using Fiji [142], we measured the minimum distance between NPCs in the high-density region of our ROI, obtaining $d_0 \approx (190 \pm 40)$ nm (mean \pm standard deviation, Table S2), close to our fitted estimates (Fig. 3(d)).

The original and post-processed image data is available at [139, DOI: 10.6019/S-BIAD2081].

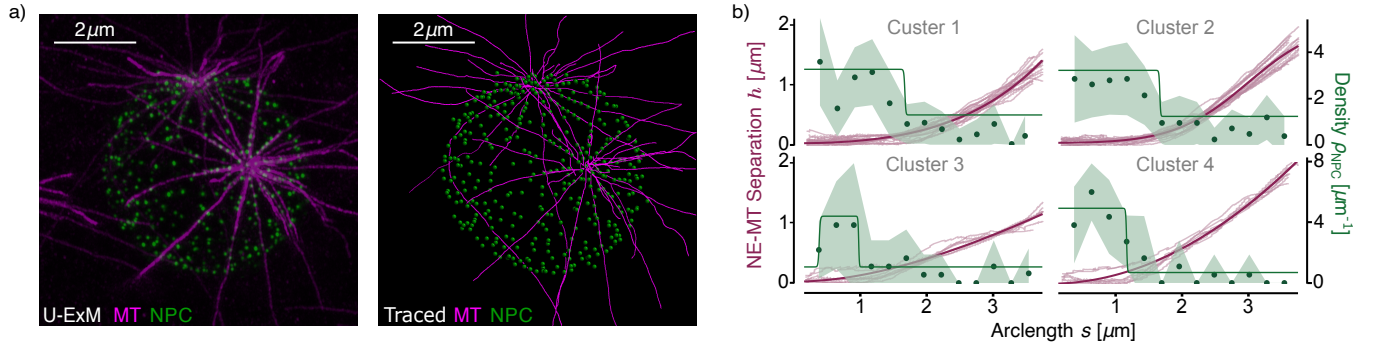


FIG. S3. Microtubules clustered according to their NE-MT separation profiles give rise to sigmoidal NPC line-densities. a) [Right] Three-dimensional rendering of microtubule traces (magenta) and NPC coordinates (green) measured from an ultrastructure expansion microscopy image [Left: 3D rendering of the original image stack] of an *S. arctica* nucleus. b) Independent fits of Eq. (6) (solid green line) to the measured NPC line-density (green dots, shaded area: 95% confidence interval) for the four MT clusters not presented in the main text, using the differentiable representation of the separation \hat{h} (dark purple) between the nuclear envelope (NE) and the microtubule (MT) filaments (individual tracks in light purple). Each fit resulted in an estimate of the separation d_0 and the effective spring constant λ .